Mineralogical and geochemical characterization of fossil bones from a Miocene marine Konservat-Lagerstätte

Bosio Giulia[1,2]*, Gioncada Anna[1], Gariboldi Karen[1], Bonaccorsi Elena[1], Collareta Alberto[1], Pasero Marco[1], Di Celma Claudio[3], Malinverno Elisa[2], Urbina Mario[4], Bianucci Giovanni[1]

[1] Dipartimento di Scienze della Terra, Università di Pisa, 56126 Pisa, Italy. giulia.bosio.giulia@gmail.com; anna.gioncada@unipi.it; karen.gariboldi@dst.unipi.it; elena.bonaccorsi@unipi.it; alberto.collareta@unipi.it; marco.pasero@unipi.it; giovanni.bianucci@unipi.it

[2] Dipartimento di Scienze dell'Ambiente e della Terra, Università degli Studi di Milano-Bicocca, 20126 Milano, Italy. giulia.bosio.giulia@gmail.com; elisa.malinverno@unimib.it

[3] Scuola di Scienze e Tecnologie, Università di Camerino, 62032 Camerino, Italy. claudio.dicelma@unicam.it

[4] Departamento de Paleontología de Vertebrados, Museo de Historia Natural, Universidad Nacional Mayor de San Marcos, Lima 1, Peru. mariourbina01@hotmail.com

Keywords: bioapatite, fossilization, East Pisco Basin, Pisco Formation, Chilcatay Formation, mammalian bone

Highlights

- Fossil vertebrates from the Pisco-Sacaco Lagerstätte are often exceptionally preserved
- Bones differ by color, mineralization degree, chemistry and presence of concretions
- Fossil bones from the same Lagerstätte underwent different fossilization paths
- Early apatite or dolomite formation mechanisms are crucial for bone preservation
- Early diagenetic minerals reduce permeability and limit bone phosphatization

Abstract

Fossil bones, together with teeth, are the most common remains of vertebrates that could manage to get preserved over geological times, providing information on the diagenetic and fossilization processes that occurred in the depositional paleoenvironment. Fossil bones from the marine vertebrate Konservat-Lagerstätte in the East Pisco Basin and Sacaco area (Peru) show a high variety of different textural and chemical features, suggestive of different processes variably contributing to the fossilization path. At the macroscopic scale, bone samples can be grouped into six different categories on the basis of the color (red to gray to white) and hardness (which relates to the mineralization degree); a variety of case studies can be found between these categories. Microscopically, the original microstructure of the bone tissue, both compact and cancellous, is well preserved in all the studied samples, with differences in cavity fillings, distribution of microcracks, and presence of Fe oxides in the diverse bone types. The bone composition and mineralogy correspond to fluorapatite. Differences in color, mineralization degree and geochemistry can be interpreted in terms of different fossilization paths, from burial at the seafloor to exposure in the present-day desert environment. The fossilization paths are strongly conditioned by the factors controlling the interplay of the mechanisms of apatite dissolution-recrystallization and dolomite precipitation (formation of carbonate concretions) and the fixation of iron in finely disseminated sulfides in the very early stages of fossilization.

1. Introduction

Made of organic and inorganic constituents, bone is a framework of calcium phosphate, similar in composition and structure to the apatite group minerals (hydroxylapatite, $Ca_{10}(PO_4)_6(OH)_2$; in a carbonate-bearing variety $(Ca,Mg,Na)_{10-x}[(PO_4)_{6-x}(CO_3)_x](OH)_{2-x}$), embedded in a protein and lipid matrix (Elliott, 2002; Wopenka and Pasteris, 2005; Pasero et al., 2010; Li and Pasteris, 2014; Fig. 1A). Fossil bone forms, with enamel, the fossil remains of vertebrates, and it can resist to decay over geological times, allowing paleontological and paleoecological reconstructions of past environments (Trueman and Tuross, 2002; Keenan, 2016). Due to the high non-mineral content (apatite is only 33-43% by volume, with the rest being made by organics and water, Olszta et al., 2007), important mineralogical, chemical and textural changes affect bones after death in order to permit preservation in the deep time, starting from the early stages after burial (from days to weeks) and continuing for years (Pfretzschner, 2004; Trueman et al., 2004, 2008; Keenan and Engel, 2017). During the early post-mortem history, collagene decay liberates apatite crystallites (Fig. 1B), which are very reactive due to their small size and crystalline structure (Keenan, 2016). Mechanisms of dissolution-recrystallization and increase in size of the apatite crystallites, reducing the surface area to volume ratio, coupled with the transformation of the Ca-phosphate from the original hydroxylapatite into the thermodynamically more stable fluorapatite, favor the preservation of the original bone histology (Elorza et al., 1999; Keenan, 2016). During the late diagenesis, further recrystallization of Ca-phosphate mineral and permineralization of the bone cavities by carbonates, sulfides, iron or manganese oxides, and silica may occur (Pfretzschner, 2004).

In the case of marine vertebrates, the post-mortem changes occurring to the fossilized bone tissue over geological timescales depend on a variety of factors, some of which are interdependent (e.g., the physical and chemical features of the sediment and seawater at the sea bottom and the presence of soft organic matter), while others are totally independent (e.g., the timing of burial and exhumation history). This complex story is recorded in form of the textural, mineralogical and chemical features of both the fossil bones and entombing deposits. Therefore, an assessment of the chemical and mineralogical characteristics of fossil bones and their host sediment can provide information on the geological and fossilization history (Hubert et al., 1996; Herwartz et al., 2013; Trueman, 2013), thus contributing to shed light on the causes behind situations of exceptional preservation (Fossil Konservat-Lagerstätten).

The Cenozoic Konzentrat- and Konservat-Lagerstätte of the East Pisco Basin and Sacaco area (Peru) displays exceptional concentrations of fossil marine vertebrates (Esperante et al., 2015;

Bianucci et al., 2016a, b), several of which are exquisitely preserved. Examples of that include digestive tract contents of cetaceans, baleen plates of mysticete whales, and skeletons of cartilaginous fishes (Esperante et al., 2008; Ehret et al., 2009, 2012; Collareta et al., 2015, 2017, 2020; Gioncada et al., 2016; Lambert et al., 2015; Marx et al., 2017). The richness of the fossil record preserved in this Lagerstätte and its extension over a rather long interval of time and through different sedimentation environments make it an ideal setting for research efforts aimed at understanding how the mineralogy and geochemistry of fossil bones can reflect different fossilization paths and processes. Nevertheless, a mineralogical and chemical study of fossil bones from this outstanding paleontological scenario is still largely lacking. The present work provides new results from field observations and petrographic, mineralogical and geochemical data regarding the bones of marine vertebrates from the Konservat-Lagerstätte of the Pisco-Sacaco Lagerstätte (southern Peru) (Esperante et al., 2015; Bianucci et al., 2016a, b). These results are then discussed with the aim of constraining the fossilization histories of bones displaying different macro- and microscopic features. Our assessment provides new clues for understanding the factors determining the preservation of the fossil marine vertebrates from the Pisco-Sacaco Lagerstätte.

2. Geological background

The tectonic evolution of Peru has been controlled, since Mesozoic times, by the convergence of the oceanic Nazca/Farallon Plate and the continental South American Plate. In correspondence of this composite transform-convergent margin, normal to strike-slip faults led to the formation of extensional/pull-apart basins along the forearc of Peru (e.g., Kulm et al., 1982; Dunbar et al., 1990; León et al., 2008). Two trench-parallel structural highs formed on the continental shelf and upper slope during the Late Cretaceous and early Paleogene times, i.e., the Outer Shelf High and the Upper Slope Ridge (Thornburg and Kulm, 1981). As a consequence of this, the Peruvian offshore is now segmented into an outer set of slope basins and an inner set of shelf basins (Fig. 2A). The East Pisco Basin is a northwest-southeast elongated shelf basin that extends for ca. 180 km along the southern Peruvian coast between the towns of Pisco and Nazca (Fig. 2A). The East Pisco Basin is placed just landward of where the aseismic Nazca Ridge (a region of topographically high and buoyant oceanic crust) impinges the Peru-Chile trench (Pilger, 1981; Hsu, 1992; Macharé and Ortlieb, 1992; Hampel, 2002) and its fill includes, in ascending stratigraphic order, the Eocene Caballas and Paracas formations, the upper Eocene Otuma Formation, the lower Miocene Chilcatay Formation, and the middle Miocene–Pliocene Pisco Formation (Dunbar et al., 1990; DeVries, 1998, 2017; DeVries et al., 2017; DeVries and Jud, 2018; Di Celma et al., 2017, 2018a, b; Solís Mundaca, 2018; Coletti et al., 2019). These sedimentary units are compositionally complex and are bounded by regionally extensive unconformities marked by pavements of pebble- to boulder-sized igneous clasts. The unconformities in-between them reflect relatively prolonged periods of subaerial exposure and, as such, they testify to major breaks of the sedimentary history of the East Pisco Basin (DeVries, 1998). As a consequence of this, the local sedimentary succession should be regarded as a series of alloformations (Di Celma et al., 2018a) as defined by the NACSN (2005).

Among the sedimentary units exposed in the East Pisco Basin, the Chilcatay and Pisco formations have been recently investigated due to the diverse and exceptionally preserved fossil vertebrate assemblages that were discovered at several sites along the western side of the lower Ica valley (Di Celma et al. 2016a, b, 2018b, 2019; Bianucci et al., 2018). During deposition of these units, the East Pisco Basin was a shallow-marine, semi-isolated embayment, sheltered eastward by a longshore chain of crystalline basement islands (i.e., the so-called “Gran Tablazo Archipelago” *sensu* DeVries and Jud, 2018) (Marocco and Muizon, 1988b; Bianucci et al., 2018). Along the Ica Valley, south of the Ocucaje village, the Chilcatay Formation is comprised of two distinct allomembers, namely, Ct1 and Ct2; the former includes three facies associations, recording deposition in shoreface (*Ct1c*), offshore (*Ct1a*), and subaqueous delta (*Ct1b*) settings, whereas the latter includes two facies associations, recording deposition in shoreface (*Ct2a*) and offshore (*Ct2b*) settings (Di Celma et al. 2018b, 2019). The overlying Pisco Formation is comprised of three fining-upward allomembers, designated P0, P1, and P2 from oldest to youngest, which progressively onlap a composite basal unconformity northeastwards. Each unit, representing a transgressive cycle, recorded deposition in shoreface (sandstones) and offshore (siltstones/diatomaceous siltstones) settings. In this area, the chronostratigraphic framework of the Chilcatay and Pisco formations is well constrained via the integration of micropaleontological data and isotope geochronology. Diatom and silicoflagellate biostratigraphy together with ^{39}Ar–^{40}Ar ages on tephra layers suggest deposition of the Chilcatay strata during the Burdigalian, between 19 and 17 Ma; the lower allomember of the Pisco Formation (P0) is dated at the Langhian-Serravallian by means of strontium isotope stratigraphy, whereas the youngest P1 and P2 allomembers are constrained between 9.5 Ma and 8.6 Ma (Tortonian), and between 8.4 and, at least, 6.7 Ma (Tortonian-Messinian), respectively, thanks to diatom biostratigraphy and ^{39}Ar–^{40}Ar ages (Gariboldi et al., 2017; Di Celma et al., 2018b; Bosio et al., 2020a, b).

Sand-prone sediments assigned to the Pisco Formation (DeVries, 2020 and references therein) also crop out in the much smaller Sacaco sub-basin, whose northern edge is encountered about 60 km south of Nazca (Fig. 2A). The Sacaco sub-basin (sometimes referred to as the "southern Pisco Basin", e.g., Ehret et al., 2012; Gariboldi et al., 2017) extends for about 50 km along the Peruvian coastline, from Lomas to Yauca (Fig. 2A). Nowadays, it is separated from the East Pisco Basin by a structural high of basement rocks that constitutes the reliefs of Monte Grande and Marcona, southeast of Nazca; so far, however, the tectonic relationships between these two areas of Neogene outcrops are still not clear, and their separation might even have followed the deposition of the Pisco Formation. In the Sacaco area, the chronostratigraphic framework is less clearly defined than in the East Pisco Basin. However, the Pisco-equivalent sediments exposed in this area have been generally regarded as younger than those of the East Pisco Basin exposed in the Ica Valley (e.g., Muizon and DeVries, 1985; Muizon, 1984, 1988; Marocco and Muizon, 1988a, b; DeVries, 2020). Following a largely biochronological approach, Muizon and DeVries (1985) and Muizon (1988) subdivided the fossiliferous succession of the Sacaco sub-basin in a number of vertebrate-bearing levels defined on the basis of their faunal composition and supported by radiometric ages (Muizon and Bellon, 1980, 1986). Such a framework provided a first rough estimate of the chronostratigraphic asset of the Pisco-equivalent strata in the Sacaco area, whose outcrops were believed to span from the lower upper Miocene (ca. 9 Ma, "El-Jahuay vertebrate level") to the lower Pliocene (ca. 4 Ma, "Sacaco vertebrate level") (Lambert and Muizon, 2013). Each vertebrate-bearing level was originally thought to encompass a single fossiliferous locality, and vice-versa; however, further field work has since clarified that the stratigraphic range of some localities is greater than that of the eponymous vertebrate level (Lambert and Muizon, 2013). Confusion between localities and vertebrate levels has thus arisen in some subsequent works (e.g., Brand et al., 2011). Moreover, U–Pb dating on zircon grains from tuff layers and Sr-isotope analyses on marine mollusk shells provided by Ehret et al. (2012) have suggested that strata exposed in the Sacaco area could be entirely referable to the upper Miocene (late Tortonian – latest Messinian) and, therefore, they seemingly originated during the same time span of the Pisco Formation in the East Pisco Basin.

3. Materials and methods

In order to account for the variability of bone preservation styles observed in the field, forty-four fossil cetacean specimens were selected for sampling among those found and described during several field surveys (2015–2019) at the localities of Cerro Colorado (14°21'01''S; 75°53'46''W), Cerro los Quesos (14°29'57''S; 75°43'06''W), Cerro la Bruja (14°31'44''S; 75°39'54''W), Pampa Corre Viento (14°27'S; 75°45'W) and Ullujaya (14°34'59''S; 75°38'27''W) in the East Pisco Basin (Fig. 2B), and Hueso Blanco (15°28'53''S; 74°48'26''W) and Montemar (15°33'28''S; 74°45'58''W) in the Sacaco sub-basin (Fig. 2C). Most of these fossil vertebrate specimens have been identified and geolocalized by Bianucci et al. (2016a, b, 2018) and Di Celma et al (2018b). A complete list of the sampled specimens is reported in Table S1.

The materials devoted to the analytical investigations include small fragments of bones (mostly rib fragments) and the host sediment (see Table S1). Sampling used the smallest amount of material necessary. Since color and hardness of fossil bones may be indicative of element uptake and apatite recrystallization and/or permineralization, we selected bones with different macroscopic colors and hardness (qualitative evaluation, comparatively estimated) for analytical follow-up. We recorded all the relevant information about the vertebrate specimen, the host sediment, and the exposure to weathering agents (see Table S1 for the complete dataset). In order to distinguish the characteristics related to the pre-exhumation history of the bones from those acquired following the exhumation and exposure to the weathering agents of the present-day desert environment (e.g., wind, sunlight, thermal excursions, night humidity...), we also collected exposed bones, avoiding bones with evidence of transport and reworking.

Twenty thin sections were prepared for petrographic investigations under the microscope, in both transmitted and reflected light. Bone fragments were embedded in epoxy resin and cut with a diamond saw. After cutting, bone slices were covered again with epoxy resin in order to fill all the empty spaces of the porous structure of the bone, and an UV resin was used for gluing the glass. Thin sections were then polished with silicon carbide and alumina.

The microanalytical investigations focused on the compact (cortical) portion of the bone (Fig. 1A). For each bone type (see below), fragments of the compact bone were mounted in epoxy, sectioned orthogonal to the bone elongation, and polished for scanning electron microscopy (SEM) and electron dispersion spectroscopy (Philips XL30 SEM equipped with DX4i EDAX microanalysis, Università di Pisa) aimed at describing their microstructural features and elemental composition, and for electron microprobe analysis (EPMA Cameca SX50, CNR, Rome) aimed at obtaining their chemical composition in terms of major and minor elements. SEM images were collected by using both secondary electrons (SE) and backscattered electrons (BSE). The SEM-EDS analytical conditions were 20 kV accelerating voltage, 5 nA beam current and 10 mm working distance. EPMA analytical conditions were 15kV accelerating voltage, 5 nA beam current, and a 10-micron defocused beam was used. Analysis of a reference apatite standard is provided in Table S2 of the Supplementary Material.

Fragments of the cortical part of four bones were visually checked under a stereomicroscope to eliminate both the exterior of the bone and any sediment clast. The bone fragments were subsequently powdered and treated with nitric and fluoridric acid digestion procedure for inductively coupled plasma mass spectrometry (ICP-MS) analyses. The concentrations of 35 trace elements were determined by using a Perkin Elmer NexION 300x spectrometer at the Università di Pisa. RGM-1 and JB-2 reference materials were also analyzed.

X-ray diffraction (XRD) analyses were carried out at the Università di Pisa. XRD analyses were performed with a Bruker D2 Phaser diffractometer, operating at 10 mA and 30 kV. Data were processed using the software DIFFRAC.EVA V4.1 for identifying the mineralogical phases.

The host sediment or rock was inspected with a stereomicroscope and examined via SEM-EDS; representative samples of different host rock types were analyzed by means of ICP-MS as described above.

4. Results

4.1. Field observations and bone macroscopic characteristics

In this work, we examined Miocene vertebrate remains of cetaceans (both odontocetes and mysticetes), which are the most represented group in the Neogene fossil record of the East Pisco Basin and Sacaco sub-basin (e.g., Muizon and DeVries, 1985; Brand et al., 2011; Bianucci et al., 2016a, b, 2018), and a few pinnipeds (see Table S1 for the complete dataset). The fossil remains of these marine vertebrates display a wide range of preservation degrees and modes. From a taphonomic point of view, the vertebrates exhibit different degrees of skeletal completeness, ranging from the preservation of more than 75% of the skeletal elements (e.g., Fig. 2D and type 2 in Fig. 3, see Table S1) to the preservation of a single skeletal element (see types 4, 5, 6 in Fig. 3). The skeletons also show different degree of articulation, ranging from 100% of articulated bones (e.g., Fig. 2D and types 1, 2, 3 in Fig. 3; see also Table S1) to fully disarticulated bones (see types 4, 5, 6 in Fig. 3, and Table S1).

The fossil remains are embedded in different kinds of variably lithified sediments, including diatomaceous mudstones and siltstones, volcanogenic or terrigenous siltstones, and fine- to coarse-grained sandstones. In some cases, the fossils are entombed within a hard, massive, tightly-cemented rock formed by carbonate concretions (i.e., a framework of diatom and/or terrigenous clasts cemented by Ca-Mg-carbonate), the latter being mostly represented by dolomite nodules as described by Gariboldi et al. (2015) (e.g., type 1 of Fig. 3). The sediment or rock surrounding the non-exposed fossil bones exhibits, till a distance of a few to ca. 30 centimeters from the bone surface, a color that differs from the rest of the sediment, being intensely reddened (see type 2 of Fig. 3) and sometimes delimited by an evident dark boundary that develops within a yellowish sediment (see type 3 of Fig. 3). This sequence, resulting from an enrichment in Fe in the red layer and in Mn in the black ones, corresponds to the yellow–black–red (YBR) sequence described by Gariboldi et al. (2015) and Gioncada et al. (2018a) in the sediments hosting the bone remains.

Based on differences in macroscopic color (dark amber, red, pearly white, white/pinkish, dark gray, white/gray-white) and hardness, bone samples were grouped into six different categories, which are described in Table 1 and illustrated in Figure 3. The white/pinkish bones of type 1 (Fig. 3) are usually fragile and easily crumbling, with the bone tissue exhibiting a low hardness, and they are embedded in a complete (type 1a) or partial (type 1c) dolomite nodule, or in volcanic ashes (type 1b). Red-colored, moderately hard bones in a loose silty/sandy sediment characterize type 2 (Fig. 3). Bones of type 3 are dark amber in color (Fig. 3), moderately hard, and hosted in scarcely cemented silty/sandy sediments made of diatoms and terrigenous (volcanoclastic) clasts. The pearly white, moderately hard bones are grouped in the type 4, whereas the white/gray-white and hard bones constitute type 5 (Fig. 3). Both types do not exhibit concretions and are hosted in Ca-carbonate-bearing clastic siltstones. Finally, bones of type 6, represented by only one sample, display the highest values of hardness in our dataset, a dark gray color (Fig. 3), and they are hosted in a loose siliciclastic sediment.

4.2. Petrography and SEM-EDS results

When observed under the transmitted light optical microscope, bone color ranges from colorless to red or reddish brown (Fig. 4). Bones of the type 2, displaying a red color in hand samples, retain a variably red to orange color also under the microscope (Fig. 4G, H). The red color of the bone tissue is usually associated to the presence of abundant Fe-oxides lining or partially filling the intertrabecular medullary cavities and interspersed in the sediment adjacent to the bone (opaques in Fig. 4G, H).

The original microstructure of the compact bone tissues is well preserved in all samples and not noticeably modified by permineralization. Bone tissues preserve the microstructure with the osteocyte lacunae and lamellae being identifiable in all the six bone types; they are particularly well-preserved in types 4, 5 and 6, and well to poorly preserved in types 1 and 2 (Fig. 4A, B). Microcracks through the bone tissue are uncommon; in some cases, they can be observed radially distributed from the Haversian canals outwards. Only in type 6, the hardest one, the bone tissue displays pervasive cracks, distributed independently from the histological microstructure of the bone (Fig. 4C).

As regards the bone tissue composition, the EDS spectra indicate that it is Ca-phosphate. Different average atomic weight in the different bone types is revealed by the grayscale of the BSE imaging (Fig. 5), which indicates different degrees of mineralization (Bloebaum et al., 1997). This is particularly evident in the difference observed between types 1 and 6 (Fig. 5A, E). Such an observation corresponds to the macroscopic evaluation of the white/pinkish bones as the softest and least mineralized type, and the dark gray bones as the hardest and most mineralized (Table 1). In type 4, the bone tissue appears more mineralized than in type 1 (Fig. 5B, C), and the Haversian canals are partially filled by newly precipitated apatite (Fig. 5D). The type 2 red-colored bones display a similar mineralization degree (Fig. 5F).

Bone cavities, i.e. the Haversian canals in the cortical bone and intertrabecular medullary cavities in the cancellous bone, might exhibit a partial or complete filling by various minerals, besides the above reported apatite (Fig. 5D), formed at different stages through early and late diagenesis. These are dolomite, iron and manganese oxides, calcite, gypsum/anhydrite.

Iron oxides can be found both in osteocyte lacunae and canaliculi (Fig. 4C inset), and/or lining intertrabecular medullary cavities (Fig. 4G, H). The opaque iron oxides filling osteocyte lacunae and canaliculi (Fig. 4C inset) typically testify the early formation of pyrite due to reducing conditions for the presence of decaying organic material (Pfretzschner, 2001a).

Micro- and cryptocrystalline dolomite can be found adjacent to the bone and filling also the microborings in the bone cortical tissue, the Haversian canals and the intertrabecular medullary cavities, in association to variable amounts of finely disseminated iron oxides (Fig. 4D; 6A, B, C). Such a carbonate occurrence and association with iron oxides, the latter being morphologically reminiscent of relics of pyrite framboids (Fig. 6C), represent evidence of the sulfate-reducing bacterial metabolic activity consequent to the decay of the organic matter in the carcass (Gariboldi et al., 2015; Gioncada et al., 2016, and references therein). Therefore, dolomite and iron oxides formed very early.

Following this interpretation, the micro- and cryptocrystalline carbonates testify to an incipient development of dolomite concretions similar to those described by Gariboldi et al. (2015) from the sediment entombing marine vertebrate skeletons of the Pisco Formation. In several cases, sediment particles (diatoms, terrigenous minerals) are present inside the bone cavities (Fig. 4E), being often separated from the bone by a thin, early-formed dolomite layer (Gariboldi et al. 2015). These sediment particles entered with seawater, possibly sucked in by the outgoing gas bubbles originated by decomposing organic matter (Bodzioch, 2015), and were then quickly cemented by the ongoing processes of dolomite formation. In some cases, the presence of sediment can be interpreted as clasts entering broken bones exposed at the seafloor before burial.

Both in the presence of the dolomite concretions and in absence of them, the residual porosity is in some cases filled by mineral phases displaying microcrystalline or coarse mosaic texture, or forming crystals with euhedral terminations in vug-like cavities (Fig. 4B, F; 6D). These are sparry calcite, Ca-sulphates (gypsum/anhydrite), and halite. While sulphates and halite are ubiquitous, calcite is common in the Chilcatay Formation at Ullujaya but extremely rare in the Pisco Formation at the localities of Cerro los Quesos and Cerro Colorado. When carbonates and sulphates coexist, textural evidence indicates that the sulphates postdate the carbonates (Fig. 6D).

4.3. X-rays diffractometry and major element chemical composition

The results of the XRPD analyses on the compact bone of the studied samples indicate the presence of apatite and minor anhydrite, dolomite and quartz. Only in type 2 (red) bones the results reveal the presence of goethite. The results of the EPMA analyses of the bone tissue in the studied samples give an F-rich Ca-phosphate composition (Table 2 and Fig. 7). The analytical totals are in the range 85-94 wt% for most bone types, with types 1, 4 and 5 showing scattered values down to 80 wt% at constant Ca/P ratios. The values of the microprobe totals are < 100 wt% due to the carbonate and hydroxyl groups in apatite mineral, which are not measured by electron microprobe, as well as to the low compactness (variable degree of mineralization) of the analyzed bone types (Fig. 7A).

The Ca/P atomic ratio broadly ranges from 1.3 to 2.1, with clustered values for each bone type with the exception of type 3 (Table 2; Fig. 7B). The Ca/P range embraces the hydroxylapatite mineral stoichiometric value and the range of published bioapatite bone materials (Ca/P= 1.67–1.78; Li and Pasteris, 2014; Wopenka and Pasteris, 2005). The highest Ca/P values are found in type 6 and are due to a gain in Ca rather than to a depletion of P. A contamination by Ca-carbonate cannot be excluded. Among the six categories in which bones were classified based on color and hardness, the dark amber (type 3) and red (type 2) bones have lower Ca/P ratios, and they exhibit higher Si, Fe and Mn abundances as well as lower F abundances than the whitish or gray ones (Fig. 7C, D, E, F; Table 2). The iron and silicon content, in particular, are higher in the bone type 2 (Table 2, S2, Fig. 7D), also in comparison with extant analyzed whale bones (Decrée et al., 2018). The Fe and Si contents are also quite high in the dark amber-colored phocid specimen of bone type

3 (Table 2, S2, Fig. 7D). The red color and the abundant iron oxides (goethite in XRPD analysis) in type 2 bones suggest that the high iron content measured with EPMA could be also the result of a contamination of the analyses by fine iron hydroxides in the bone tissue microporosity.

4.4. Trace element geochemistry

Four samples of well-preserved fossil bones, representative of different situations in terms of development of concretions and mineralization degrees of the bone tissue (see Table 1), and four samples of sediment were selected for the trace element analysis. The bone samples are: CC-M63 of the type 1a, within a dolomite nodule; CLQ-M3 of the type 1b, without nodule but with a Mn-Fe boundary layer; CC-M28 of the type 2, strongly mineralized, without nodule but with a Mn-Fe boundary layer, exhibiting Fe enrichment; and MT-M1 of the type 6: strongly mineralized, without nodule, without Fe enrichment.

The redox-sensitive elements Cu, Fe, U vary in abundance among the different bone types (Table 3). In particular, U is present with comparatively higher values in specimens MT-M1 of type 6 (250 ppm) and CC-M28 of type 2 (45 ppm). Ni (121 ppm), Zn (451 ppm), and Mo (30 ppm) are comparatively higher in the bone sample with the highest Fe content (CC-M28 of the type 2), with values that are higher than those reported for extant marine mammals (Decrée et al. 2018).

The REE content of the analyzed bones is ΣREE = 6–60 ppm, in the lower range of fossil bone REEs (1–10,000 ppm) but remarkably higher than the bone REE concentrations in living organisms, ranging from 0.001 to 1 ppm (Trueman and Tuross, 2002). The REE patterns, reported in Figure 8 after normalization to the PAAS, are variably fractionated, with high HREE up to PAAS-normalized values >1, and low La_N/Yb_N ratio except for the bone sample from within a dolomitic nodule, in which the La_N/Yb_N ratio equals 0.8. Overall, the samples display La_N/Sm_N and La_N/Yb_N ratios close to the field of seawater (Fig. 9). All the samples exhibit a positive Gd anomaly and positive Y peak. In turn, the Ce anomaly is low or absent.

5. Discussion

5.1. Processes of mineralization responsible of bone fossilization in the Pisco-Sacaco Lagerstätte

The studied fossil bone samples display a broad variability of color and hardness values and, based on these, have herein been grouped into six different categories, exhibiting different physical and chemical characteristics. Overall, these different groups depict a continuum of different macroscopic aspects of the bone that can be found in different fossil specimens or even within a same fossil specimen.

In the studied samples, the bone tissue consists of Ca-phosphate and no examples of substitution of apatite by other phases (e.g., crystalline or amorphous silica or pyrite) has been detected. Carbonates, iron sulphides and Ca-sulphates formed at different stages, and in the red-colored bones the bone tissue is permeated with minute Fe-oxides (e.g., the brighter areas in Figure 5F), but none of these minerals remarkably replaced the original biogenic apatite. Therefore, both the hardness of the studied fossil bones and the preservation degree of the histological structures must depend on the degree of apatite recrystallization (Fig. 1B), whereas color must depend on element uptake from the local environment and fine iron sulfides precipitation. These mechanisms, on their hand, are influenced by the chemical-physical conditions of porewater (oxygen level, availability of P, Fe, S, Mn) during the very early stages of the fossilization history (pre-burial and burial stages, Fig. 10), which determine the element availability and the nature of the newly formed minerals.

Sea floor oxygen availability, abundance of organic matter, and sediment permeability and composition are crucial factors controlling the mineral formation in early diagenesis, immediately after burial (Fig. 10). With respect to the Pisco-Sacaco Lagerstätte vertebrates, the marine sediments in which the carcasses were buried are variably permeable, potentially allowing chemical exchange between the bone and seawater shortly after burial. The least permeable lithologies are the thin, fine-grained tephra layers. Therefore, the aerobic oxidation of the organic matter could be favored. However, the oxygen level at the seafloor was low and occasionally very low (suboxic to anoxic conditions), especially in the offshore environment, as a consequence of the abundant decaying organic matter made available by high productivity waters, and due to the limited circulation of waters in the East Pisco Basin (Bianucci et al., 2018). The Miocene situation was probably similar to that observed in the present-day Peruvian and Chilean slope (Manheim et al., 1975; Rhoads et al., 1991; Emeis et al., 1991; Böning et al., 2004) and in protected bays of the currently submerged portions of the East Pisco Basin (i.e., the Paracas Bay, Aguirre-Velarde et al., 2019). Just below the sediment-seawater boundary, the low O_2 availability and the abundance of organic matter provided by the buried vertebrate carcasses could activate processes of Fe, Mn and sulphate reduction (SBR) shortly after burial (Allison, 1988; Briggs, 2003; Shapiro and Spangler, 2009). The microbial or inorganic reduction of Fe and Mn oxyhydroxides liberates into the porewater the surface-bound phosphate subtracted from the water column (Creveling et al., 2014). Coupled with the phosphorous addition provided by the decay of the organic matter, this P availability promotes the Ca-phosphate mineral recrystallization thanks to the lowering of pH within the apatite dissolution-recrystallization window due to the first products of organic matter decay (Berna et al., 2004). The stability of apatite depends on P availability, pH and the type of phosphate mineral, being carbonate-bearing F-apatite more stable than hydroxylapatite in slightly acidic and low P solutions (Keenan, 2016). Thus, bone preservation is highly dependent on this early process of apatite recrystallization and bone phosphatization (Fig. 1B).

On the other hand, bacterial sulfate reduction increases both the abundance of bicarbonate ions and pH, favoring carbonate minerals formation; at the same time, it lowers sulfate concentration, an inhibiting factor for dolomite stability, thus triggering the precipitation of dolomite (Allison, 1988; Briggs and Wilby, 1996; Shapiro and Spangler, 2009; Gariboldi et al., 2015; Gioncada et al., 2018b). At a very early stage, a crucial role is, therefore, played by the chemical-physical properties of porewater for what concerns the conditions favoring Ca-phosphate formation (and bone mineralization) and/or carbonate cement formation (and thus development of dolomite concretions around the bones). Both these processes are pivotal for bone preservation because they may occur very early, and even during the syn-burial stage (Fig. 10), while the organic matter is decomposing

(Meister et al., 2011; Muramiya et al., 2020). They affect preservation in a complex way: while the rapid decrease of permeability induced by the early concretion formation limits the decay of organic matter by slowing the interaction with the oxidants (McCoy et al., 2015), it may also limit the availability of P for apatite recrystallization and bone phosphatization. Thus, it can be envisaged that the early formation of concretions (Fig. 10) demonstrated at Cerro Colorado and Cerro los Quesos rapidly reduced the permeability necessary for element uptake from porewater, which limited phosphatization, and as such, bone mineralization (Gariboldi et al. 2015). Bone mineralization by Ca-phosphate is, indeed, found to be higher in samples without the early dolomite concretion (Gioncada et al., 2018a).

Given the above described framework, the characteristics of the studied bones provide information on the spectrum of processes controlling the degree of apatite recrystallization, element uptake, and mineral precipitation from porewater that occurred during the early diagenesis, the late diagenesis and the much later exposure in the present-day desert environment. Figure 10 summarizes these processes and the factors controlling them, while Figure 11 displays the proposed connection between the variety of characteristics displayed by the fossil bones and the processes they encountered. Carbonate nodules formed very early, and their presence indicates that the fossilization conditions changed rapidly from those favorable for apatite recrystallization to those favorable for nucleation of carbonates; the bones retain a white-pinkish color (type 1, Fig. 11), and are fragile and prone to break. Bones preserved in a sediment without nodule may have been subject to a prolonged apatite recrystallization, providing a dark amber color and a moderate hardness to the bone tissue (type 3, Fig. 11). Bones can acquire an intense red color due to Fe-hydroxides permeating the bone tissue. Iron precipitates as pyrite framboid precursors within the sediment and the bone cavities under reducing conditions in the early stages of the organic matter decay and diagenesis, as a by-product of the Fe and sulfate reduction mechanisms (Pfretzschner, 2000b, 2001a; Vietti et al., 2015), and it is then fixed in form of hydroxides following oxidation (Pfretzschner, 2001b) (goethite in type 2, Fig. 11). Mn may also precipitate at redox or pH boundaries. During the late diagenesis, secondary minerals, such as carbonates, anhydrite and halite, precipitated and filled the bone cavities. In type 6 (Fig. 11), the high hardness of the bone is accompanied by both a high Ca content of the bone tissue and a pervasive precipitation of large-sized calcite crystals in the osteons and intertrabecular medullary cavities. Pervasive polygonal microcracks through the bone tissue, preceding the calcite filling, are ascribed to the external stresses in the late diagenetic phase, whereas the radially distributed microcracks around the osteons are to be ascribed to the early diagenetic phase (Pfretzschner, 2000a, 2004). Finally, during the exposure in the present-day desert environment, fossil bones can be bleached and weakened by exogenous agents removing the fine iron oxides and changing their color, resulting in pearly white to gray, moderately hard bones (types 4 and 5, Fig. 11).

5.2 Chemical-physical conditions of the fossilization stages

The bones of marine vertebrates of the Pisco Formation consist of fluorapatite and are not affected by relevant processes of permineralization by minerals other than Ca-phosphate. Differences in the totals of microprobe analyses, in Ca/P values, and in Fe and Si contents indicate, however, the existence of diverse compositions in the analyzed bones (Fig. 7). Remarkable differences are also highlighted by the trace element contents in U, Zn, Ni, and REE revealed by four of the studied bones (Fig. 8, Table 3).

The higher values of U are to be attributed to enrichment during diagenesis, in the presence of reducing solutions in which U is soluble (Pfretzschner, 2000b; Keenan et al., 2015). Ni, Zn and Mo are comparatively higher in the bone sample with higher Fe contents, which suggests that the sediment hosting the bones was enriched in these elements during sedimentation in oxic conditions, because Ni and Zn are adsorbed onto Fe-Mn particles that form in oxic seawater. Similarly, these particles scavenge from seawater also REE, in particular LREE (Light REE) (Trueman and Tuross, 2002; Keenan et al., 2015).

During fossilization, REE are taken by the newly formed apatite as substitutes for Ca (Trueman and Tuross, 2002). Firstly, REE uptake depends, therefore, on the composition, pH and redox conditions of the porewater during early diagenesis. On the other hand, the final REE patterns are the result of the long-term diffusion in fossil bones and depend, therefore, on the late diagenetic stages (Herwartz et al., 2013; Kowal-Linka et al., 2014). Thus, REE patterns may fingerprint the paleoenvironment shortly after burial only if they are not overprinted by later diagenetic, hydrothermal or metamorphic events. In the marine environment, mechanisms that determine fractionation and the final REE patterns of fossil bones are complex, but the most relevant include the preferential LREE sorption on bone apatite crystallites as well as the LREE sorption on reactive Fe-Mn oxides and hydroxides (Chen et al., 2015); the latter instance enhances the HREE mobility, thus allowing the HREE to reach the inner parts of the bone (Herwartz et al., 2013). The REE patterns of bones in Figure 8 indicate low and variable REE uptake. The fractionated patterns of three out of four samples and their Gd and Y anomalies strongly recall the influence of oxic seawater (see the low La/Yb ratio, and the positive La, Gd and Y anomalies of Pacific seawater; De Baar et al., 1985), although the lack of any Ce anomaly suggests conditions similar to seawater at the depth of oxygen minimum, i.e., ca. 150 to 200 m (Fig. 8). This is in agreement with the overall suboxic condition at seafloor in the East Pisco Basin, which could be linked to a high oxygen consumption due to high productivity (see paragraph 5.1) as well as to a scarcely efficient exchange with oxygenated oceanic water due to the basin physiography (as has been recently observed for the extant Paracas Bay; Aguirre-Velarde et al., 2019).

Moreover, the similarities with the seawater field in Figure 9 indicate that the bones acquired their REE imprint during early diagenesis of marine sediments and that there is no evidence for prolonged diagenetic or metamorphic processes. Only the bones inside a nodule display a scarcely fractionated pattern: this can be explained with early fossilization occurring in locally anoxic conditions due to anaerobic decay of organic matter that caused sulfate reduction, as well as nitrate and Mn-Fe reduction and uptake of LREE formerly scavenged by Fe-Mn particles. The early diagenetic anoxic (sulfidic) conditions likely resulted by organic matter decay consuming oxygen while exchange with oxic seawater was limited by early burial (Gariboldi et al., 2015; McCoy et al., 2015). The formation of a dolomite nodule reduced permeability and consequently limited later modifications of the REE pattern by oxic seawater. The resulting REE pattern corresponds, in fact, to that developing in a sulfate reduction environment (Fig. 9) (see Kim et al., 2012). However, according to Kim et al. (2012), Fe-reduction would cause a MREE bulge in the porewater pattern that is not visible in our bone pattern. The bone found in sediment rich in volcanic ash has the lowest REE contents, although the pattern is similar to that of seawater. Among the different sediment types hosting the bones of the Pisco Formation, volcanic ash is the least permeable, thus probably limiting prolonged interaction with seawater. All the bones without a nodule retain the pattern of seawater, which suggests REE uptake in oxic-suboxic conditions, with relatively low oxygen availability. The highly porous sediment, such as sandstones, allows bones to exchange with the porewater fluids (Gioncada et al., 2018a). The lack of any Eu anomaly is in agreement with the lack of interaction with high temperature, reducing, chloride-rich hydrothermal fluids (Michard, 1989).

6. Conclusions

The fossil bones of marine vertebrates of the Pisco-Sacaco Lagerstätte witness a broad variety of preservation modes, which at the macroscale reflect into different features such as color, hardness and the presence/absence of embedding carbonate concretions. In many cases, the bone tissue displays well preserved histological details at the microscopic scale, such as osteocyte lacunae and lamellae, revealing that processes of phosphatization were active along with the decay of the organic part of the bone tissue during the earliest steps of diagenesis. This prevented the later access of fluids which could favor bone substitution by diagenetic minerals other than apatite. Fe-oxide framboids (former iron sulfides) and microcrystalline dolomite are also early diagenetic minerals. Red-colored bones exhibit abundant Fe oxides in the intertrabecular medullary cavities, preceding late diagenetic minerals and therefore indicating abundant iron sulfide formation during early diagenesis, also within the bone tissue microporosity. Finally, late minerals such as gypsum/anhydrite and halite may partially fill cracks and bone cavities, irrespective of the presence or absence of external dolomite concretions.

In absence of dolomite nodule, the siliciclastic sands or silts in which bones are deposited constitute a highly permeable environment where bones can react and exchange elements with the porewater fluids. As a consequence of this, they record a trace element and REE pattern similar to seawater. On the other hand, bones deposited within volcanic ashes or embedded into early diagenetic dolomite nodules experience low permeability conditions, limiting the trace elements and REE uptake.

Our data indicate that two main mineral formation mechanisms, both active in the early diagenetic stages, appear to have controlled the mineralization and preservation of the bone tissue during fossilization, namely, the dissolution-recrystallization of apatite and the development of a dolomite concretion enclosing the bone. The macroscopic color of the bone before exposure to weathering is mainly connected to oxidation of early diagenetic iron sulfides.

The herein results indicate that future works on bones might hopefully shed new light on the correlation between the physical and chemical characteristics of the bones and their fossilization paths. Bone preservation is determined by independent and interdependent factors and agents that act at different times, and it ultimately reflects the early fossilization, sheltering, and late post-mortem history.

Acknowledgements

The authors are grateful to F. Colarieti and M. Serracino for their experienced help with analytical work. The authors would like to thank R. M. Varas-Malca, W. Aguirre, and J. A. Chauca Luyo for the support during the fieldwork, and O. Lambert, C. de Muizon, and F. G. Marx for the interesting discussions on marine vertebrates. The authors wish to thank two anonymous reviewers and the Editor F. J. Vega for their useful and constructive comments.

Funding

This study was supported by grants from the Italian Ministero dell'Istruzione dell'Università e della Ricerca (PRIN Project 2012YJSBMK) and the Università di Pisa (PRA_2015_0028 and PRA_2017_0032).

References

Aguirre-Velarde, A., Thouzeau, G., Jean, F., Mendo, J., Cueto-Vega, R., Kawazo-Delgado, M., Vásquez-Spencer, J., Herrera-Sanchez, D., Vega-Espinoza, A., Flye-Sainte-Marie, J., 2019. Chronic and severe hypoxic conditions in Paracas Bay, Pisco, Peru: Consequences on scallop growth, reproduction, and survival. Aquaculture, 512, 734259. https://doi.org/10.1016/j.aquaculture.2019.734259.

Allison, P.A., 1988. The Role of Anoxia in the Decay and Mineralization of Proteinaceous Macro-Fossils. Paleobiology, 14, 2, 139–154.

Berna, F., Matthews, A., Weiner, S., 2004. Solubilities of bone mineral from archaeological sites: the recrystallization window. Journal of Archaeological Science, 31, 867–882.

Bianucci, G., Collareta, A., Bosio, G., Landini, W., Gariboldi, K., Gioncada, A., Lambert, O., Malinverno, E., Muizon, C. de, Varas-Malca, R., Villa, I.M, Coletti, G., Urbina, M., Di Celma, C., 2018. Taphonomy and palaeoecology of the lower Miocene marine vertebrate assemblage of Ullujaya (Chilcatay Formation, East Pisco Basin, southern Peru). Palaeogeography Palaeoclimatology Palaeoecology, 511, 256–279. https://doi.org/10.1016/j.palaeo.2018.08.013.

Bianucci, G., Di Celma, C., Collareta, A., Landini, W., Post, K., Tinelli, C., Muizon, C. de, Bosio, G., Gariboldi, K., Gioncada, A., Malinverno, E., Cantalamessa G., Altamirano-Sierra, A, Salas-

Gismondi, R., Urbina, M., Lambert, O., 2016a. Fossil marine vertebrates of Cerro Los Quesos: Distribution of cetaceans, seals, crocodiles, seabirds, sharks, and bony fish in a late Miocene locality of the Pisco Basin, Peru. Journal of Maps, 12, 1037–1046. https://doi.org/10.1080/17445647.2015.1115785.

Bianucci, G., Di Celma, C., Landini, W., Post, K., Tinelli, C., Muizon, C. de, Gariboldi, K., Malinverno, E., Cantalamessa, G., Gioncada, A., Collareta, A., Salas-Gismondi, R., Varas-Malca, R.M., Urbina, M., Lambert, O., 2016b. Distribution of fossil marine vertebrates in Cerro Colorado, the type locality of the giant raptorial sperm whale Livyatan melvillei (Miocene, Pisco Formation, Peru). Journal of Maps, 12, 543–557. https://doi.org/10.1080/17445647.2015.1048315, 2016b.

Bloebaum, R.D., Skedros, J.G., Vajda, E.G., Bachus, K.N., Constantz, B.R., 1997. Determining mineral content variations in bone using backscattered electron imaging. Bone, 20, 485–490. https://doi.org/10.1016/S8756-3282(97)00015-X.

Bodzioch, A., 2015. Idealized Model of Mineral Infillings in Bones of Fossil Freshwater Animals, on the Example of Late Triassic Metoposaurs from Krasiejów (Poland). Austin Journal of Earth Science, 2(1), 1008.

Böning, P., Brumsack, H.J., Böttcher, M.E., Schnetger, B., Kriete, C., Kallmeyer, J., Borchers, S.L., 2004. Geochemistry of Peruvian near-surface sediments. Geochimica et Cosmochimica Acta, 68, 21, 4429–4451.

Bosio, G., Malinverno, E., Collareta, A., Di Celma, C., Gioncada, A., Parente, M., Berra, F., Marx, F.G., Vertino, A., Urbina, M., Bianucci, G., 2020a. Strontium Isotope Stratigraphy and the thermophilic fossil fauna from the middle Miocene of the East Pisco Basin (Peru). Journal of South American Earth Sciences, 97, 102399. https://doi.org/10.1016/j.jsames.2019.102399.

Bosio, G., Malinverno, E., Villa, I.M., Di Celma, C., Gariboldi, K., Gioncada, A., Barberini, B., Urbina, M., Bianucci, G., 2020b. Tephrochronology and chronostratigraphy of the Miocene

Chilcatay and Pisco formations (East Pisco Basin, Peru). Newsletters on Stratigraphy, in press. https://doi.org/10.1127/nos/2019/0525.

Brand, L.R., Urbina, M., Chadwick, A., DeVries, T.J., Esperante, R., 2011. A high resolution stratigraphic framework for the remarkable fossil cetacean assemblage of the Miocene/Pliocene Pisco Formation, Peru. Journal of South American Earth Sciences, 31, 414–425. https://doi.org/10.1016/j.jsames.2011.02.015.

Briggs, D.E.G., 2003. The Role of Decay and Mineralization in the Preservation of Soft-Bodied Fossils. Annual Review of Earth and Planetary Sciences, 31, 275–301. https://doi.org/10.1146/annurev.earth.31.100901.144746.

Briggs, D.E.G., Wilby, P.R., 1996. The role of the calcium carbonate-calcium phosphate switch in the mineralization of soft-bodied fossils. Journal of the Geological Society, 153, 665–668.

Chen, J., Algeo, T. J., Zhao, L., Chen, Z. Q., Cao, L., Zhang, L., Li, Y., 2015. Diagenetic uptake of rare earth elements by bioapatite, with an example from Lower Triassic conodonts of South China. Earth-Science Reviews, 149, 181–202. http://dx.doi.org/10.1016/j.earscirev.2015.01.013

Coletti, G., Bosio, G., Collareta, A., Malinverno, E., Bracchi, V., Di Celma, C., Basso, D., Stainbank, S., Spezzaferri, S., Cannings, T., Bianucci G., 2019. Biostratigraphic, evolutionary, and paleoenvironmental significance of the southernmost lepidocyclinids of the Pacific coast of South America (East Pisco Basin, southern Peru). Journal of South American Earth Sciences, 96, 102372. https://doi.org/10.1016/j.jsames.2019.102372.

Collareta, A., Landini, W., Chalcatana, C., Valdivia, W., Altamirano-Sierra, A., Urbina- Schimtt, M., Bianucci, G., 2017. A well preserved skeleton of the fossil shark *Cosmopolitodus hastalis* from the late Miocene of Peru, featuring fish remains as fossilized stomach contents. Riv. Ital. Paleontol. Stratigr. 123, 11–22.

Collareta, A., Landini, W., Lambert, O., Post, K., Tinelli, C., Di Celma, C., Panetta, D., Tripodi, M., Salvadori, P.A., Caramella, D., Marchi, D., Urbina, M., Bianucci, G., 2015. Piscivory in a Miocene Cetotheriidae: first record of fossilized stomach content for an extinct baleen-bearing whale. Sci. Nat. 102 article #70.

Collareta, A., Tejada-Medina, L., Chacaltana-Budiel, C., Landini, W., Altamirano-Sierra, A., Urbina-Schmitt, M., Bianucci, G. 2020. A rhinopristiform sawfish (genus *Pristis*) from the middle Eocene (Lutetian) of southern Peru and its regional implications. Carnets Geol., 20(5), 91–105.

Creveling, J. R., Johnston, D. T., Poulton, S. W., Kotrc, B., März, C., Schrag, D. P., Knoll, A. H. 2014. Phosphorus sources for phosphatic Cambrian carbonates. GSA Bulletin, 126(1-2), 145–163.

De Baar, H.J., Bacon, M.P., Brewer, P.G., Bruland, K.W., 1985. Rare earth elements in the Pacific and Atlantic Oceans. Geochimica et Cosmochimica Acta, 49, 1943–1959. https://doi.org/10.1016/0016-7037(85)90089-4.

Decrée, S., Herwartz, D., Mercadier, J., Miján, I., de Buffrénil, V., Leduc, T., Lambert, O. 2018. The post-mortem history of a bone revealed by its trace element signature: The case of a fossil whale rostrum. Chemical Geology, 477, 137–150.

DeVries, T.J., 1998. Oligocene deposition and Cenozoic sequence boundaries in the Pisco Basin (Peru). J. South Am. Earth Sci. 11, 217–231. https://doi.org/10.1016/S0895-9811(98)00014-5.

DeVries, T.J., 2017. Eocene stratigraphy and depositional history near Puerto Caballas (East Pisco Basin, Peru). Boletín de la Sociedad Geológica del Perú, 112, 39–52.

DeVries, T.J., 2020. Lithostratigraphy and biostratigraphy of Pliocene and Pleistocene marine deposits and age of the highest marine terrace from the Sacaco Basin and its environs (southern Peru). Boletín de la Sociedad Geológica del Perú, 114, 20–48.

DeVries, T.J., Jud, N.A., 2018. Lithofacies patterns and paleogeography of the Miocene Chilcatay and lower Pisco depositional sequences (East Pisco Basin, Peru). Boletín de la Sociedad Geológica del Perú, Volumen Jubilar 8, 124–167.

DeVries, T.J., Urbina, M., Jud, N.A., 2017. The Eocene-Oligocene Otuma depositional sequence (East Pisco Basin, Peru): Paleogeographic and paleoceanographic implications of new data. Boletín de la Sociedad Geológica del Perú, 112, 14–38

Di Celma, C., Malinverno, E., Bosio, G., Collareta, A., Gariboldi, K., Gioncada, A., Molli, G., Basso, D., Varas-Malca, R.M., Pierantoni, P.P., Villa, I.M., Lambert, O., Landini, W., Sarti, G., Cantalamessa, G., Urbina, M., Bianucci, G., 2017. Sequence stratigraphy and paleontology of the upper Miocene Pisco Formation along the western side of the lower Ica valley (Ica Desert, Peru). Rivista Italiana di Paleontologia e Stratigrafia, 123, 255–274. https://doi.org/10.13130/2039-4942/8373.

Di Celma, C., Malinverno, E., Bosio, G., Gariboldi, K., Collareta, A., Gioncada, A., Landini, W., Pierantoni, P.P., Bianucci, G., 2018a. Intraformational unconformities as a record of late Miocene eustatic falls of sea level in the Pisco Formation (southern Peru). Journal of Maps, 14, 607–619. https://doi.org/10.1080/17445647.2018.1517701.

Di Celma, C., Malinverno, E., Cantalamessa, G., Gioncada, A., Bosio, G., Villa, I.M., Gariboldi, K., Rustichelli, A., Pierantoni, P.P., Landini, W., Tinelli, C., Collareta, A., Bianucci, G., 2016a. Stratigraphic framework of the late Miocene Pisco Formation at Cerro Los Quesos (Ica Desert, Peru). Journal of Maps, 12, 1020–1028. https://doi.org/10.1080/17445647.2015.1115783.

Di Celma, C., Malinverno, E., Collareta, A., Bosio, G., Gariboldi, K., Lambert, O., Landini, W., Gioncada, A., Villa, I.M., Coletti, G., Muizon, C. de, Urbina, M., Bianucci, G., 2018b. Facies analysis, stratigraphy and marine vertebrate assemblage of the early Miocene Chilcatay Formation at Ullujaya (Pisco basin, Peru). J. Maps 14, 257–268. https://doi.org/10.1080/17445647.2018.1456490.

Di Celma, C., Malinverno, E., Gariboldi, K., Gioncada, A., Rustichelli, A., Pierantoni, P.P., Landini, W., Bosio, G., Tinelli, C., Bianucci, G., 2016b. Stratigraphic framework of the late Miocene to Pliocene Pisco Formation at Cerro Colorado (Ica Desert, Peru). J. Maps 12, 515–557. https://doi.org/10.1080/17445647.2015.1047906.

Di Celma, C., Pierantoni, P.P., Malinverno, E., Collareta, A., Lambert, O., Landini, W., Bosio, G., Gariboldi, K., Gioncada, A., Muizon, C. de, Molli, G., Marx, F.G., Varas-Malca, R.M., Urbina, M., Bianucci, G., 2019. Allostratigraphy and paleontology of the lower Miocene Chilcatay Formation in the Zamaca area, East Pisco basin, southern Peru. J. Maps 15, 393–405. https://doi.org/10.1080/17445647.2019.1604439.

Dunbar, R.B., Marty, R.C., Baker, P.A., 1990. Cenozoic marine sedimentation in the Sechura and Pisco basins, Peru. Palaeogeogr. Palaeoclim. 77, 235–261.

Ehret, D.J., Hubbell, G., MacFadden, B.J. 2009. Exceptional preservation of the white shark Carcharodon (Lamniformes, Lamnidae) from the early Pliocene of Peru. Journal of Vertebrate Paleontology, 29, 1–13. https://doi.org/10.1671/039.029.0113.

Ehret, D.J., Macfadden, B.J., Jones, D.S., DeVries, T.J., Foster, D.A., Salas-Gismondi, R., 2012. Origin of the white shark Carcharodon (Lamniformes: Lamnidae) based on recalibration of the Upper Neogene Pisco Formation of Peru. Palaeontology, 55, 1139–1153. https://doi.org/10.1111/j.1475-4983.2012.01201.x.

Elliott, J.C., 2002. Calcium phosphate biominerals. Reviews in Mineralogy and Geochemistry, 48(1), 427-453.

Elorza, J.; Astibia, H.; Murelaga, X.; Pereda-Suberbiola, X., 1999. Francolite as a diagenetic mineral in dinosaur and other Upper Cretaceous reptile bones (Laño, Iberian Peninsula): microstructural, petrological and geochemical features. Cretaceous Research 20: 169187. doi:10.1006/cres.1999.0144.

Emeis, K.C., Whelan, J.K., Tarafa, M. 1991. Sedimentary and geochemical expressions of oxic and anoxic conditions on the Peru shelf. Geological Society, London, Special Publications, 58(1), 155–170.

Esperante, R., Brand, L., Nick, K.E., Poma, O., Urbina, M., 2008. Exceptional occurrence of fossil baleen in shallow marine sediments of the Neogene Pisco Formation, Southern Peru. Palaeogeogr. Palaeoclimatol. Palaeoecol. 257, 344–360.

Esperante, R., Brand, L.R., Chadwick, A.V., Poma, O., 2015. Taphonomy and paleoenvironmental conditions of deposition of fossil whales in the diatomaceous sediments of the Miocene/Pliocene Pisco Formation, southern Peru - a new Fossil-Lagerstätte. Palaeogeography Palaeoclimatology Palaeoecology, 417, 337–370. https://doi.org/10.1016/j.palaeo.2014.09.029.

Gariboldi, K., Bosio, G., Malinverno, E., Gioncada, A., Di Celma, C., Villa, I.M., Urbina, M., Bianucci, G., 2017. Biostratigraphy, geochronology and sedimentation rates of the upper Miocene Pisco Formation at two important marine vertebrate fossil-bearing sites of southern Peru. Newsletters on Stratigraphy, 50, 417–444. https://doi.org/10.1127/nos/2017/0345.

Gariboldi, K., Gioncada, A., Bosio, G., Malinverno, E., Di Celma, C., Tinelli, C., Cantalamessa, G., Landini, W., Urbina, M., Bianucci, G., 2015. The dolomite nodules enclosing fossil marine vertebrates in the East Pisco Basin, Peru: field and petrographic insights into the Lagerstätte formation. Palaeogeography Palaeoclimatology Palaeoecology, 438, 81–95. https://doi.org/10.1016/j.palaeo.2015.07.047, 2015.

Gioncada, A., Collareta, A., Gariboldi, K., Lambert, O., Di Celma, C., Bonaccorsi, E., Urbina, M., Bianucci, G., 2016. Inside baleen: exceptional microstructure preservation in a late Miocene whale skeleton from Peru. Geology 44, 839–842.

Gioncada, A., Gariboldi, K., Collareta, A., Di Celma, C., Bosio, G., Malinverno, E., Lambert, O., Pike, J., Urbina, M., Bianucci, G., 2018a. Looking for the key to preservation of fossil marine vertebrates in the Pisco Formation of Peru: new insights from a small dolphin skeleton. Andean Geology 45, 379–398.

Gioncada, A., Petrini, R., Bosio, G., Gariboldi, K., Collareta, A., Malinverno, E., Bonaccorsi, E., Di Celma, C., Pasero, M., Urbina, M., Bianucci, G., 2018b. Insights into the diagenetic environment of fossil marine vertebrates of the Pisco Formation (late Miocene, Peru) from mineralogical and Sr-isotope data. Journal of South American Earth Sciences, 81, 141-152. https://doi.org/10.1016/j.jsames.2017.11.014.

Hampel, A., 2002. The migration history of the Nazca Ridge along the Peruvian active margin: A re-evaluation and some geological implications. Earth and Planetary Science Letters, 203, 665–679.Herwartz, D., Tütken, T., Jochum, K. P., Sander, P. M., 2013. Rare earth element systematics of fossil bone revealed by LA-ICPMS analysis. Geochimica et Cosmochimica Acta, 103, 161–183. https://doi.org/10.1016/j.gca.2012.10.038.

Hsu, J.T., 1992. Quaternary uplift of the Peruvian coast related to the subduction of the Nazca Ridge: 13.5 to 15.6 degrees South latitude. Quaternary International 15/16, 87–97. https://doi.org/10.1016/1040-6182(92)90038-4.

Hubert, J.F., Panish, P.T., Chure, D.J., Prostak, K.S. 1996. Chemistry, microstructure, petrology, and diagenetic model of Jurassic dinosaur bones, Dinosaur National Monument, Utah. Journal of Sedimentary Research, 66(3), 531-547.

Keenan, S.W., 2016. From bone to fossil: A review of the diagenesis of bioapatite. American Mineralogist, 101, 1943–1951. https://doi.org/10.2138/am-2016-5737.

Keenan, S.W., Engel, A.S., 2017. Early diagenesis and recrystallization of bone. Geochimica et Cosmochimica Acta, 196, 209–223. https://doi.org/10.1016/j.gca.2016.09.033.

Keenan, S.W., Engel, A.S., Roy, A., Bovenkamp-Langlois, G.L., 2015. Evaluating the consequences of diagenesis and fossilization on bioapatitelattice structure and composition. Chemical Geology, 413, 18–27.

Kim, J.H., Torres, M.E., Haley, B.A., Kastner, M., Pohlman, J.W., Riedel, M., Lee, Y.J. (2012). The effect of diagenesis and fluid migration on rare earth element distribution in pore fluids of the northern Cascadia accretionary margin. Chemical Geology, 291, 152–165.

Kowal-Linka, M., Jochum, K.P., Surmik, D., 2014. LA-ICP-MS analysis of rare earth elements in marine reptile bones from the Middle Triassic bonebed (Upper Silesia, S Poland): Impact of long-lasting diagenesis, and factors controlling the uptake. Chemical Geology, 363, 213–228.

Kulm, L.D., Resig, J.M., Thornburg, T.M., Schrader, H.J., 1982. Cenozoic structure, stratigraphy 928 and tectonics of the central Peru forearc. In: Legget, J.K. (Ed.), Trench and forearc geology: sedimentation and tectonics on modern and ancient plate margins. London, Blackwells, 151–169. https://doi.org/10.1144/GSL.SP.1982.010.01.10.

Lambert, O., Collareta, A., Landini, W., Post, K., Ramassamy, B., Di Celma, C., Urbina, M., Bianucci, G. 2015. No deep diving: evidence of predation on epipelagic fish for a stem beaked whale from the Late Miocene of Peru. Proceedings of the Royal Society B: Biological Sciences, 282(1815), 20151530. https://doi.org/10.1098/rspb.2015.1530.

Lambert, O., Muizon, C. de, 2013. A new long-snouted species of the Miocene pontoporiid dolphin Brachydelphis and a review of the Mio-Pliocene marine mammal levels in the Sacaco Basin, Peru. Journal of Vertebrate Paleontology, 33, 709–721. https://doi.org/10.1080/02724634.2013.74340513.743405.

León, W., Aleman, A., Torres, V., Rosell, W., de la Cruz, O. 2008. Estratigrafía, sedimentología y evolución tectónica de la cuenca Pisco Oriental. Boletín INGEMMET, ser. D., 27, 1–144.

Li, Z., Pasteris, J.D., 2014. Chemistry of bone mineral, based on the hypermineralized rostrum of the beaked whale Mesoplodon densirostris. American Mineralogist, 99, 645–653. https://doi.org/10.2138/am.2014.4571

Macharé, J., Ortlieb, L., 1992. Plio-Quaternary vertical motions and the subduction of the Nazca Ridge, central coast of Peru. Tectonophysics, 205, 97–108. https://doi.org/10.1016/0040-1951(92)90420-B.

Manheim, F., Rowe, G.T., Jipa, D. 1975. Marine phosphorite formation off Peru. Journal of Sedimentary Research, 45(1), 243–251. https://doi.org/10.1306/212F6D20-2B24-11D7-8648000102C1865D

Marocco, R., Muizon, C. de, 1988a. Los vertebrados del Neogeno de la costa sur del Perú: ambiente sedimentario y condiciones de fosilización. Bulletin de l'Institut Français d'études Andines, 17, 105–117.

Marocco, R., Muizon, C. de, 1988b. Le Bassin Pisco, bassin cénozoïque d’avant arc de la côte du Pérou central: analyse géodynamique de son remplissage. Géodynamique, 3, 3–19.

Marx, F.G., Collareta, A., Gioncada, A., Post, K., Lambert, O., Bonaccorsi, E., Urbina, M., Bianucci, G., 2017a. How whales used to filter: exceptionally preserved baleen in a Miocene cetotheriid. J. Anat. 231, 212–220.

McCoy, V.E., Young, R.T., Briggs, D.E.G., 2015. Sediment permeability and the preservation of soft-tissues in concretions: An experimental study. Palaios, 30, 608–612.

Meister, P., Gutjahr, M., Frank, M., Bernasconi, S.M., Vasconcelos, C., McKenzie, J.A. 2011. Dolomite formation within the methanogenic zone induced by tectonically driven fluids in the Peru accretionary prism. Geology, 39(6), 563-566.

Michard, A., 1989. Rare earth element systematics in hydrothermal fluids. Geochimica et Cosmochimica Acta, 53, 745–750. https://doi.org/10.1016/0016-7037(89)90017-3.

Muizon C. de., 1984. Les Vertébrés de la Formation Pisco (Pérou). Deuxième partie: Les Odontocètes (Cetacea, Mammalia) du Pliocène inférieur de Sud-Sacaco. Travaux de l'Institut Français d'Études Andines, 27, 1-188.

Muizon, C. de, 1988. Les Vertébrés de la Formation Pisco (Pérou). Troisième partie: Les Odontocètes (Cetacea, Mammalia) du Miocène. Travaux de l'Institut Français d'Études Andines, 42, 1–244.

Muizon, C. de, Bellon, H., 1980. L'âge mio-pliocène de la Formation Pisco (Pérou). Comptes Rendus Hebdomadaires des Séances de l'Académie des Sciences de Paris, Série D, 290, 1063–1066.

Muizon, C. de, DeVries, T.J., 1985. Geology and paleontology of late Cenozoic marine deposits in the Sacaco area (Peru). Geologische Rundschau, 74, 547–563. https://doi.org/10.1007/BF01821211.

Muramiya, Y., Yoshida, H., Kubota, K., Minami, M. 2020. Rapid formation of gigantic spherical dolomite concretion in marine sediments. Sedimentary Geology, 105664.

North American Commission on Stratigraphic Nomenclature [NACSN], 2005. North American stratigraphic code. AAPG (American Association of Petroleum Geologists) Bulletin, 89, 1547–1591.

Olszta, M.J., Cheng, X., Jee, S.S., Kumar, R., Kim, Y.Y., Kaufman, M.J., Douglas, E.P., Gower, L.B., 2007. Bone structure and formation: A new perspective. Materials Science and Engineering: R: Reports, 58, 77–116. https://doi.org/10.1016/j.mser.2007.05.001.

Pasero, M., Kampf, A.R., Ferraris, C., Pekov, I.V., Rakovan, J., White, T.J., 2010. Nomenclature of the apatite supergroup minerals. European Journal of Mineralogy, 22, 163–179. https://doi.org/10.1127/0935-1221/2010/0022-2022.

Pilger, R.H., 1981. Plate reconstructions, aseismic ridges, and low-angle subduction beneath the Andes. Geologica Society of America Bulletin, 92, 448–456. https://doi.org/10.1130/0016-7606(1981)92<448:PRARAL>2.0.CO;2.

Pfretzschner, H.U., 2000a. Microcracks and fossilization of Haversian bone. Neues Jahrbuch für Geologie und Paläontologie-Abhandlungen, 413–432.

Pfretzschner, H.U., 2000b. Pyrite formation in Pleistocene bones-a case of very early mineral formation during diagenesis. Neues Jahrbuch für Geologie und Paläontologie-Abhandlungen, 143–160.

Pfretzschner, H.U., 2001a. Pyrite in fossil bone. Neues Jahrbuch für Geologie und Paläontologie-Abhandlungen, 1–23.

Pfretzschner, H.U., 2001b. Iron oxides in fossil bone. Neues Jahrbuch für Geologie und Paläontologie-Abhandlungen, 417–429.

Pfretzschner, H.U., 2004. Fossilization of Haversian bone in aquatic environments. Comptes Rendus Palevol, 3, 605–616. https://doi.org/10.1016/j.crpv.2004.07.006.

Rhoads, D.C., Mulsow, S.G., Gutschick, R., Baldwin, C.T., Stolz, J.F. 1991. The dysaerobic zone revisited: a magnetic facies? Geological Society, London, Special Publications, 58(1), 187–199.

Shapiro, R.S., Spangler, E. 2009. Bacterial fossil record in whale-falls: petrographic evidence of microbial sulfate reduction. Palaeogeography, Palaeoclimatology, Palaeoecology, 274(3-4), 196–203.

Solís Mundaca, F.A., 2018. Bioestratigrafía e implicancias paleoceanográficas de las diatomeas de la sección Cerro Caucato, Formación Pisco, Ica, Perù. Master Thesis, Universidad Peruana Cayetano Heredia, Lima, Peru, 125 pp.

Thornburg, T.M., Kulm, L.D., 1981. Sedimentary basins of the Peru continental margin: structure, stratigraphy, and Cenozoic tectonics from 6ºS to 16ºS latitude. In: Kulm, L.D., Dymond, J., Dasch, E.J., Hussong, D.M. (Eds.), Nazca plate: crustal formation and Andean convergence. Geological Society of America Memoir, 154, 393–422.

Trueman, C.N., Tuross, N., 2002. Trace elements in recent and fossil bone apatite. Reviews in Mineralogy and Geochemistry, 48, 489–521. https://doi.org/10.2138/rmg.2002.48.13.

Trueman, C.N., Behrensmeyer, A.K., Tuross, N., Weiner, S., 2004. Mineralogical and compositional changes in bones exposed on soil surfaces in Amboseli National Park, Kenya: diagenetic mechanisms and the role of sediment pore fluids. Journal of Archaeological Science, 31(6), 721–739. https://doi.org/10.1016/j.jas.2003.11.003.

Trueman, C.N., 2013. Chemical taphonomy of biomineralized tissues. Palaeontology, 56(3), 475-486. https://doi.org/10.1111/pala.12041

Trueman, C.N., Privat, K., Field, J., 2008. Why do crystallinity values fail to predict the extent of diagenetic alteration of bone mineral? Palaeogeography, Palaeoclimatology, Palaeoecology, 266, 160–167. https://doi.org/10.1016/j.palaeo.2008.03.038.

Vietti, L.A., Bailey, J.V., Fox, D.L., Rogers, R.R., 2015. Rapid formation of framboidal sulfides on bone surfaces from a simulated marine carcass fall. Palaios, 30(4), 327–334. http://dx.doi.org/10.2110/palo.2014.027

Wopenka, B., Pasteris, J.D., 2005. A mineralogical perspective on the apatite in bone. Materials Science and Engineering: C, 25, 131–143. https://doi.org/10.1016/j.msec.2005.01.008.

Zúñiga-Rivero, F.J., Klein, G.D., Hay-Roe, H., Álvarez-Calderon, E., 2010. The hydrocarbon potential of Peru. Lima, BPZ.

Figure captions

Figure 1. Bone structure and microstructure. A. Bone structure in cross section. The bone tissue can be distinguished into the outer compact bone and the inner cancellous bone. The compact bone

is an external layer composed by elemental units called osteons, at the center of which are the Haversian canals that host blood vessels and nerves. The compact bone is covered by an outer membrane called periosteum. The cancellous bone (trabecular or spongy bone) comprises the internal tissue of the bone and it is formed by the trabeculae, elemental units that partition the inner portion of the bone into intertrabecular medullary cavities where the bone marrow is stored. See the schematic bioapatite unit of the bone tissue at the bottom right of the figure. **B.** Sketch illustrating the main transformations that bone bioapatite undergoes during fossilization. The first step is the loss of the OM (i.e., Organic Matter), which leaves pore spaces in which diagenetic fluids can circulate. These fluids enriched in dissolved ions allow the replacement of Ca^{2+}, OH^{-}, PO_4^{3-} in the apatite lattice, while favoring the recrystallization of apatite and precipitation of new apatite with consequent reduction of porosity in the bone. Redrawn and modified after Keenan (2016).

Figure 2. Geographical and paleontological setting. A. Geographical setting of the East Pisco Basin and Sacaco sub-basin in the Ica and Arequipa regions (Peru). **B.** Satellite image and positions of the investigated localities of the East Pisco Basin: Cerro Colorado, Pampa Corre Viento, Cerro los Quesos, Cerro la Bruja and Ullujaya, along the western side of the Ica River. **C.** Satellite image and positions of the investigated localities of the Sacaco Basin: Hueso Blanco and Montemar near Puerto Lomas. **D.** An investigated fossil specimen (CC-M11) of a mysticete baleen whale in the desert environment of the Ica desert along the Peruvian coast.

Figure 3. Examples of vertebrate bone types. Fossil bones investigated in the Ica Desert have been classified into six different types (1 to 6) based on their macroscopic characteristics (see Table 1).

Figure 4. Bone photomicrographs. A. Compact bone of the specimen CLQ-M3 (type 1b, see Table 1) in transmitted plane-polarized light showing the preserved original microstructure (i.e., primary and secondary osteons, lamellae and osteocyte lacunae). **B.** Compact bone of the specimen CLQ-M1 (type 1c) in reflected light, showing the preserved original microstructure (i.e., lamellae). Note that the Haversian canals are filled by a sparry dolomitic cement. **C.** Compact bone of the

specimen MT-M1 (type 6) in transmitted plane-polarized light, showing preserved lamellae and osteocyte lacunae, as well as pervasive fractures. In the bottom-left inset, osteocyte lacunae and canaliculi filled with iron oxides are shown. Note the pervasive and polygonal microcracks cutting the osteons, and the carbonate filling of the Haversian canals. **D.** Cancellous bone of the specimen CLQ-M10 (type 1c) in transmitted plane-polarized light, showing microborings from bacterial activity in the outer surface of the bone. Dolomite cement is present inside the microborings, in the intertrabecular medullary cavities, and in the surrounding diatomaceous sediment. **E.** Cancellous bone of the specimen CC-M22 (type 1c) exhibiting a very fragile bone tissue and sediment particles (terrigenous grains and volcanic glasses) filling the bone cavities. These particles entered in the bone cavities along with seawater, probably by being sucked in as a consequence of the escaping of gas bubbles originated during decay of the organic matter. **F.** Compact bone of the specimen MT-M1 (type 6) in transmitted cross-polarized light, showing the mosaic carbonate cement filling of the Haversian canals precipitated during the late diagenesis. **G.** Cancellous bone of the specimen CC-M11 (type 2), showing the bright red color of the bone visible both macroscopically and under the microscope. Note that the intertrabecular medullary cavities are filled by Fe-oxides, the ghosts of framboidal pyrite. Fe-oxides can fill the whole cavity or exhibit secondary filling in the center. **H.** Detail of a blood vessel cavity of the specimen CC-M11 (type 2), exhibiting spherules of Fe-oxides, the ghosts of framboidal pyrite, which strictly adhere to the bone tissue. The center of the cavity is filled by secondary anhydrite.

Figure 5. SEM-BSE images of fossil bones. A. Compact bone of the specimen CC-M63 (type 1a) exhibiting fragile and not permineralized bone tissue. Note the radial cracks around the osteons. **B.** Compact bone of the specimen UL-O5 (type 4) exhibiting a moderately hard tissue. Note the cracks that are present around the osteons, and that some Haversian canals in the center of the image are partially filled by apatite. **C.** Close-up of the bone tissue and osteocyte lacunae of the specimen UL-O5 (type 4) displaying a scarce permineralization. **D.** Close-up of a Haversian canal of the specimen UL-O5 (type 4) displaying apatite filling, precipitated during fossilization. **E.** Compact

bone of the specimen MT-M1 (type 6), exhibiting a highly mineralized tissue. **F.** Compact bone of the specimen CC-M28 (type 2), showing a highly mineralized tissue and brighter areas suggesting Fe-oxide grains in the bone tissue. Note the different average atomic weight (different shades of grey) in the diverse bone types, revealing a different degree of permineralization.

Figure 6. SEM-BSE images of the cements filling the bone cavities. A. Compact (external) and cancellous (internal) bone of the mysticete specimen CLQ-M67. Note the dolomite filling the bone cavities (both Haversian canals and intertrabecular medullary cavities) and the microborings, the latter being referable to the "type C" (*sensu* Gariboldi et al. 2015). **B.** Close-up of a bone trabecula of the odontocete specimen UL-O5. Note the different generations of dolomite (dark grey) occurring near the bone tissue, and calcite in the center of the bone cavity. **C.** Close-up of a framboidal Fe-oxide, ghost of a pyrite framboid, in the dolomite cement embedding and filling the bone of the specimen CLQ-M67. **D.** Close-up of cancellous bone of the odontocete specimen UL-O41, showing calcite cement filling the intertrabecular medullary cavities, with a fracture filled secondarily by gypsum.

Figure 7. EPMA compositional diagrams of bone apatite. Values are shown as atoms per formula unit.

Figure 8. REE analyses on fossil bones. REE spidergrams for four bone samples, volcanic ashes, and diatomaceous sediments of the Lagerstätte. The REE patterns of seawater at different depths are also shown. All data are normalized to the PAAS.

Figure 9. $(La/Yb)_N$ vs $(La/Sm)_N$ of the analyzed bones compared to the REE ratios in seawater. Paths produced by processes acting in early and protracted diagenesis and metamorphism are also indicated.

Figure 10. Processes and factors acting during the post-mortem history of a whale. Scheme of the processes and factors that affect bones from the fall of the whale carcass to its complete burial and later exposure in a modern desert environment (inspired by Keenan, 2016).

Figure 11. Bone type processes and characterization. Scheme of the processes that take place during burial, early and late diagenesis, and exposure in a modern desert environment, with the bone characterization for each bone type identified in the Pisco-Sacaco Fossil-Lagerstätte.

Table captions

Table 1. Fossil bone types obtained on the basis of macroscopic characteristics (color and relative hardness, sediment type and presence of concretions) observed in East Pisco and Sacaco fossil bones.

Table 2. Mean, number of analyses (in brackets) and standard deviation (SD) of the electron microprobe analyses of bone, for the different types individuated in this work; bdl: below detection limit; FeOtot: all Fe as FeO. Formula recalculated based on 13 total anions and 1 (F, Cl, OH). M sites with 1+ and 2+ cations and T sites with 4+, 5+ and 6+ cations (Pasero et al., 2010).

Table 3. Trace element chemical composition of fossil bones and sediment samples, obtained by means of ICP-MS. "A" stands for cortical bone, "B" for diatomaceous sediment, and "C" for volcanic ash; bdl: below detection limit; nd: not determined.

Supplementary Material

Table S1. Complete dataset of the fossil bones analyzed for this work in the East Pisco Basin and Sacaco sub-basins. Hueso Blanco and Montemar are localities from the Sacaco area. All the other localities are from the Ica River Valley.

Table S2. Complete dataset of electron microprobe analyses of fossil bones. See text for analytical details.

Table 1

Type	Description		Representative samples and *specimen***	Host sediment	Mineral cement or concretion
	color	hardness*			
1	white/pinkish	low hardness	1a: 11 [*CC-M63]*	1a: diatomaceous silt	dolomite concretion
		low hardness, fragile	1b: 2 [*CLQ-M3]*	1b: tephra	no dolomite concretion
		low hardness, easily crumbling	1c: M1A [*CLQ-M1]*, M10A [*CLQ-M10]*, M50A [*CLQ-M50],* CCA86 *[CC-M22]*	1c: diatomaceous silt/mudstone	variable development of dolomite concretion
2	red	moderately hard, fragile	12, 30 *[CC-M28]*	diatomaceous silt/sand, deformed by the load of the carcass	no concretion, but a Mn-Fe boundary is visible under the specimen (Fig. 3)
3	dark amber	moderately hard	3a: CCB86 *[CC-P7]*	silt/sand	specimen in a scarcely cemented nodule, no dolomite
4	pearly white	moderately hard	37 [*UL-O41]*, 48 [*UL-O5]*, D12 [*UL-O66]*	siliciclastic sand with carbonatic fraction	no
5	white/gray-white	hard/very hard	49 [*HB-1]*, 51 [*HB-3]*	sand	no
6	dark gray	very hard	52 [*MT-M1]*	sand	no

* relative hardness, comparative estimation

**specimen to which the bone samples belong is in square brackets; details can be found in Table S1

Table 2

	Type 1		Type 2		Type 3a		Type 3b		Type 4		Type 5		Type 6	
	mean [5]	SD	mean [12]	SD	mean [14]	SD	mean [9]	SD	mean [14]	SD	mean [7]	SD	mean [4]	SD
SiO_2 wt%	0.11	0.12	1.12	0.49	2.45	1.12	0.01	0.01	0.01	0.01	bdl	0.01	0.01	0.01
MgO	0.49	0.11	2.53	1.32	1.81	0.22	1.09	0.09	0.37	0.10	0.64	0.32	0.53	0.05
CaO	45.14	2.38	32.12	4.21	40.59	2.28	47.92	0.80	47.97	2.26	47.88	3.31	50.89	0.27
MnO	0.01	0.02	0.12	0.03	0.09	0.03	0.09	0.02	0.02	0.02	0.02	0.02	0.02	0.02
FeOtot	0.04	0.03	17.32	6.96	4.55	1.42	0.10	0.03	0.05	0.11	0.04	0.04	0.08	0.05
Na_2O	1.37	0.17	1.30	0.30	1.06	0.17	1.10	0.07	1.28	0.16	1.25	0.07	0.91	0.10
SrO	0.13	0.05	0.07	0.08	0.13	0.05	0.13	0.05	0.13	0.09	0.04	0.04	0.22	0.11
PbO	bdl	-	0.01	0.02	bdl	-	bdl	-	bdl	-	bdl	-	0.01	0.02
P_2O_5	31.48	0.76	27.28	2.51	33.14	0.90	34.74	0.59	32.93	1.31	33.82	2.33	31.01	0.36
SO_3	2.78	0.23	2.74	0.53	2.64	0.35	3.31	0.08	3.00	0.26	2.82	0.38	2.06	0.51
F	1.41	0.27	1.36	0.25	1.58	0.41	3.40	0.59	2.29	0.42	2.39	0.63	1.95	0.32
Cl	0.86	0.21	0.87	0.38	0.67	0.21	0.12	0.03	0.42	0.29	0.35	0.15	0.33	0.07
H_2O_{calc}	0.59		0.57		0.66		0.00		0.36		0.35		0.51	
Total	84.42		87.42		89.38		92.01		88.86		89.60		88.53	
Formula proportions based on 13 total anions and 1 (F, Cl, OH)														
Si	0.011		0.116		0.232		0.001		0.001		0.000		0.001	
Mg	0.074		0.392		0.259		0.150		0.053		0.091		0.078	
Ca	4.889		3.578		4.114		4.742		4.950		4.878		5.379	
Mn	0.001		0.011		0.007		0.007		0.002		0.002		0.002	
Fe	0.004		1.506		0.360		0.008		0.004		0.003		0.007	
Na	0.269		0.262		0.194		0.197		0.239		0.230		0.174	
Sr	0.008		0.004		0.007		0.007		0.007		0.002		0.013	
Pb	0.000		0.000		0.000		0.000		0.000		0.000		0.000	
P	2.694		2.401		2.654		2.717		2.685		2.722		2.590	
S	0.211		0.214		0.187		0.229		0.217		0.201		0.153	
F	0.451		0.447		0.473		0.993		0.698		0.719		0.608	
Cl	0.147		0.153		0.107		0.019		0.069		0.056		0.055	
OH	0.401		0.398		0.419		0.000		0.233		0.225		0.336	
M site	5.244		5.754		4.938		5.111		5.255		5.206		5.653	
T site	2.916		2.732		3.073		2.947		2.903		2.924		2.744	
Ca/P	1.81		1.49		1.55		1.75		1.84		1.79		2.08	

Table 3

Sample	11	30-01	ESP-2	52	CLQ20-Q	CLQ20-P	CLQ20-N	CLQT8-T4	CLQT8-base	CLQT8-T6	CLQT8-tephra
material	A	A	A	A	B	B	B	B	B	B	C
Li	1.53	4.00	2.59	1.66	52	48	23.9	3.9	20.9	7.9	0.64
Be	0.48	3.05	0.31	2.50	0.68	0.66	0.93	2.90	0.86	2.75	3.32
Ga	1.04	1.26	1.05	1.38	10.0	9.6	9.9	13.9	10.5	14.0	14.8
Rb	0.58	1.97	0.78	0.67	56	50	48	116	58	115	139
Sr	758	551	1060	1423	155	169	217	100	663	100	78
Y	7.4	235	4.2	21.5	4.6	4.5	8.6	12.3	5.0	12.2	13.4
Zr	11.0	22.1	33.0	87	68	67	94	120	66	118	128
Nb	0.34	0.44	0.31	0.44	5.5	5.1	6.0	12.9	5.7	12.4	14.5
Mo	2.92	51	9.7	2.60	5.9	5.5	4.1	5.2	66	5.8	2.96
Cs	0.03	0.14	0.03	0.07	5.1	4.5	3.6	4.3	4.9	4.7	4.3
Ba	27.5	52	49	81	219	206	315	734	504	683	785
La	5.0	5.7	1.00	4.0	9.8	10.4	15.6	47	24.0	43	52
Ce	7.7	8.2	1.28	4.4	17.5	18.3	29.6	86	51	78	95
Pr	0.84	1.10	0.17	0.40	2.01	2.11	3.5	8.7	5.8	8.0	9.7
Nd	3.22	4.8	0.88	1.46	7.1	7.4	13.0	27.5	18.4	25.3	30.0
Sm	0.62	1.34	0.23	0.42	1.16	1.22	2.30	3.9	2.01	3.8	4.2
Eu	0.12	0.38	0.06	0.12	0.29	0.29	0.56	0.60	0.44	0.58	0.60
Gd	0.74	4.7	0.38	1.01	0.93	0.90	1.83	2.40	1.03	2.29	2.43
Tb	0.11	0.75	0.06	0.19	0.14	0.13	0.27	0.38	0.16	0.36	0.39
Dy	0.73	6.7	0.47	1.60	0.82	0.83	1.56	2.23	0.92	2.08	2.30
Ho	0.17	2.43	0.13	0.44	0.17	0.16	0.31	0.43	0.18	0.40	0.45
Er	0.51	9.5	0.45	1.64	0.49	0.48	0.85	1.23	0.52	1.15	1.28
Tm	0.08	1.40	0.06	0.30	0.08	0.07	0.12	0.19	0.08	0.18	0.20
Yb	0.48	8.5	0.39	2.22	0.50	0.47	0.79	1.27	0.52	1.15	1.35
Lu	0.08	2.02	0.08	0.39	0.08	0.07	0.12	0.19	0.08	0.18	0.21
Hf	0.09	0.16	0.37	0.40	2.14	2.10	2.6	4.0	1.97	3.7	4.2
Ta	0.01	0.03	bdl	0.01	0.39	0.40	0.45	1.13	0.43	1.04	1.24
W	0.41	0.89	0.18	0.34	0.66	0.64	0.60	1.02	0.67	0.98	1.07
Pb	bdl	3.7	4.1	5.0	6.6	7.0	10.3	24.0	22.9	23.0	23.2

Th	0.29	0.34	0.04	0.11	4.5	4.5	4.6	19.4	7.2	17.9	22.1
U	7.7	24.0	1.46	250	2.00	1.96	1.63	4.8	4.9	4.9	4.9
Sc	0.97	1.39	1.83	2.50	4.3	4.9	4.3	3.8	4.4	5.3	2.7
V	3.3	29.7	13.2	28.1	87	112	63	22.2	109	45	5.2
Cr	4.2	14.0	7.4	9.3	47	42	23.2	10.6	65	24.9	4.7
Co	1.74	19.4	3.6	1.28	8.5	11.0	6.5	1.09	3.28	1.66	0.46
Ni	2.19	121	42	1.49	100	105	44	4.9	19.2	8.5	2.42
Cu	nd	32.4	14.8	421	21.7	31.4	20.6	5.1	37	14.1	nd
Zn	38	451	145	102	555	322	326	41	139	137	45

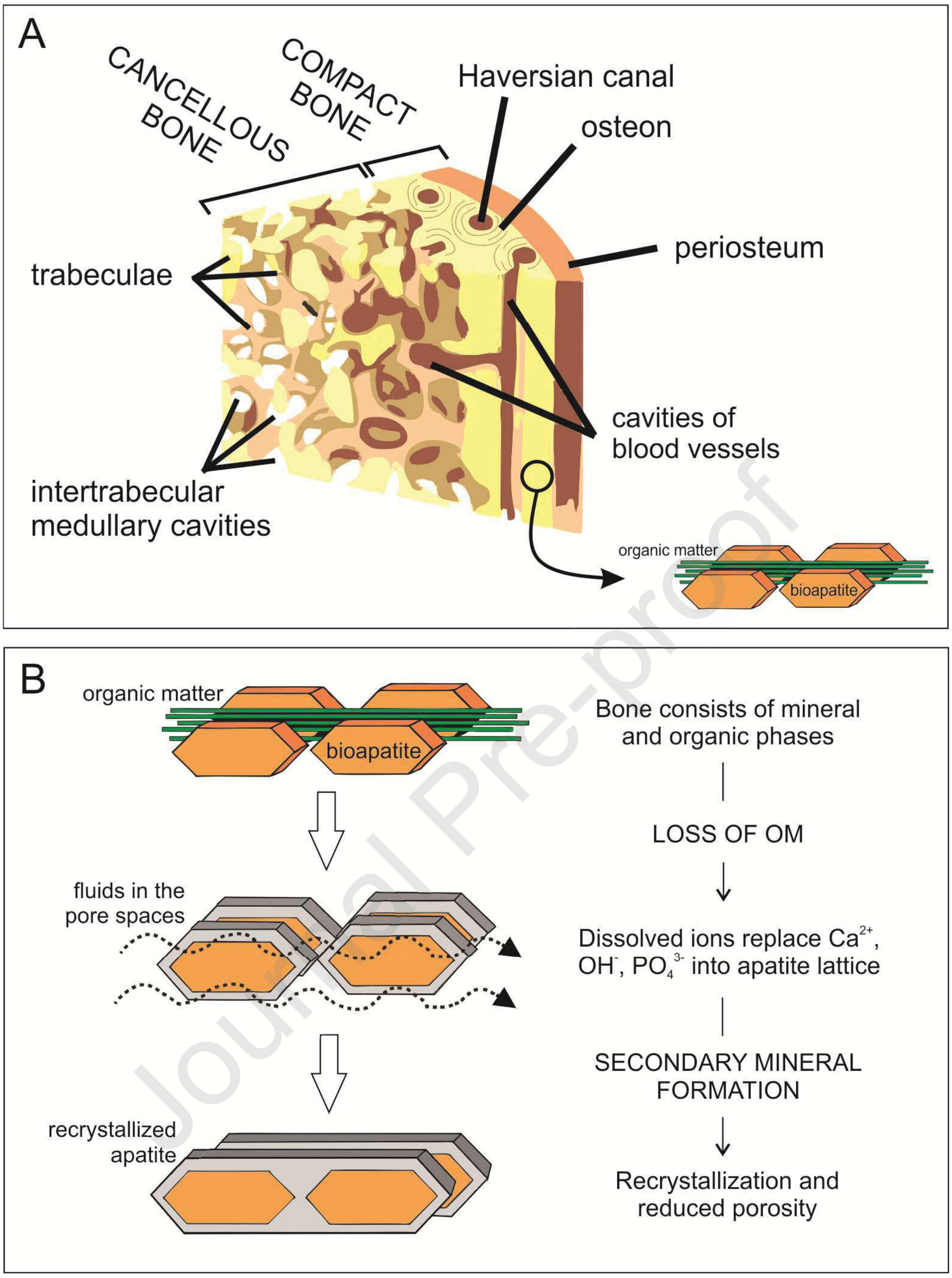
A
CANCELLOUS BONE
COMPACT BONE
Haversian canal
osteon
periosteum
trabeculae
cavities of blood vessels
intertrabecular medullary cavities
organic matter
bioapatite
B
organic matter
bioapatite
Bone consists of mineral and organic phases
LOSS OF OM
fluids in the pore spaces
Dissolved ions replace Ca2+, OH-, PO43- into apatite lattice
SECONDARY MINERAL FORMATION
recrystallized apatite
Recrystallization and reduced porosity

Figure 1

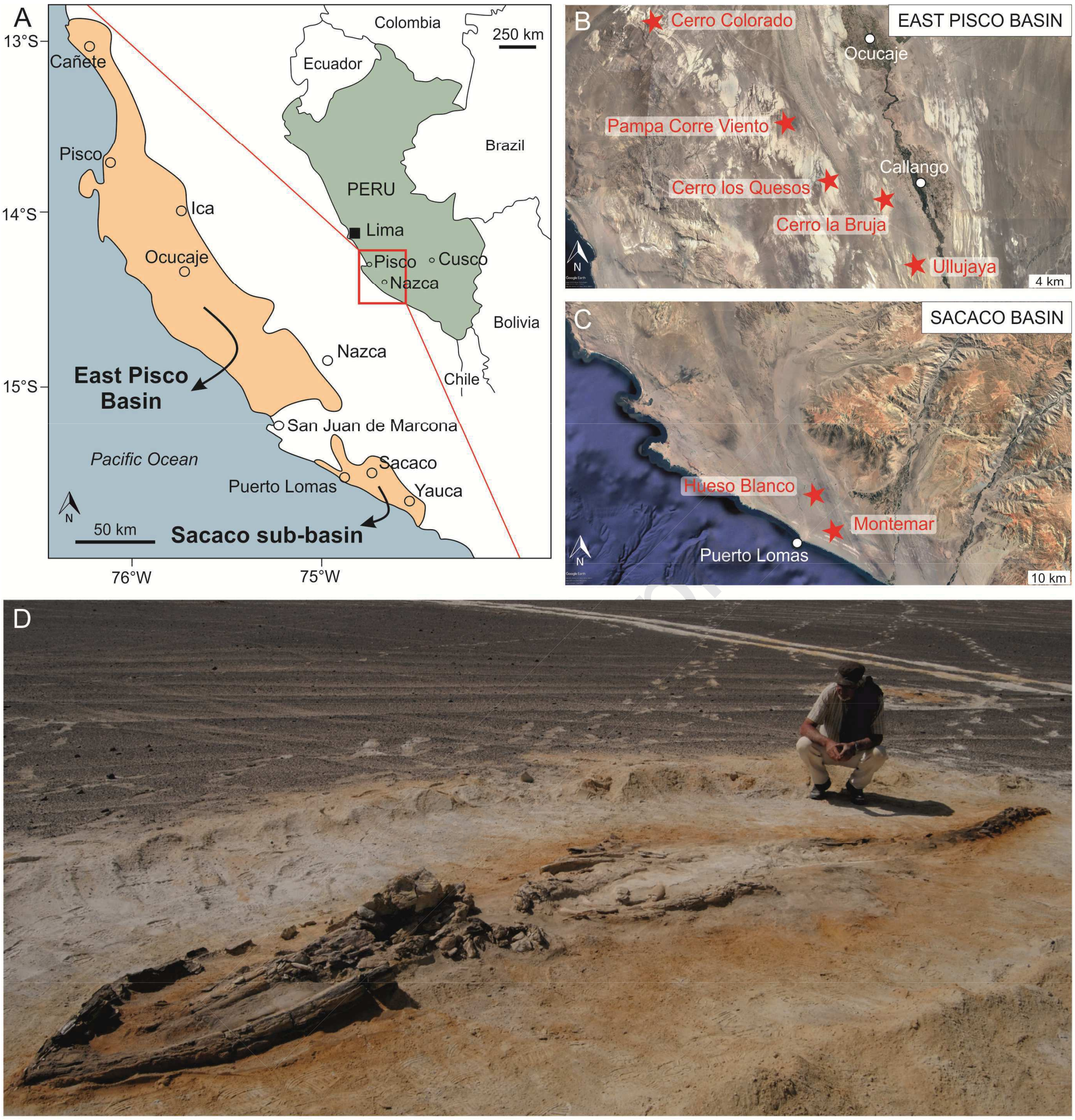

965

966 **Figure 2**

967

Type 1

CC-M22: cranium and articulated mandibles of small baleen whale (Cetotheriidae) from Pisco Fm, Cerro Colorado (East Pisco Basin)

Note the dolomite concretion originally fully embedding the fragile and white bones

Type 2

CC-M28: articulated skeleton of small baleen whale (Cetotheriidae) from Pisco Fm, Cerro Colorado (East Pisco Basin)

Note the red bones embedded in the diatomaceous silt reddened near the skeleton

Type 3

MUSM 887: partially articulated skeleton of small dolphin (*Brachydelphis mazeasi*) from Pisco Fm, Pampa Corre Viento (East Pisco Basin)

Note the dark and well mineralized bones delimited by a black boundary layer in yellowish sand

Type 4

UL-81(MUSM 2527): cranium of longirostral dolphin (*Chilcacetus cavirhinus*) from Chilcatay Fm, Ullujaya (East Pisco Basin)

Note the pearly white bones inside well consolidated grey sand

Type 5

HB-3: rib fragment of indeterminate cetacean from Pisco Fm, Hueso Blanco (Sacaco sub-basin)

Note the eroded white bone exposed in the desertic environment

Type 6

MT-M1: fragment of an isolated rib of indeterminate cetacean from Pisco Fm, Montemar (Sacaco sub-basin)

Note the dark color of the well mineralized bone

Figure 3

970

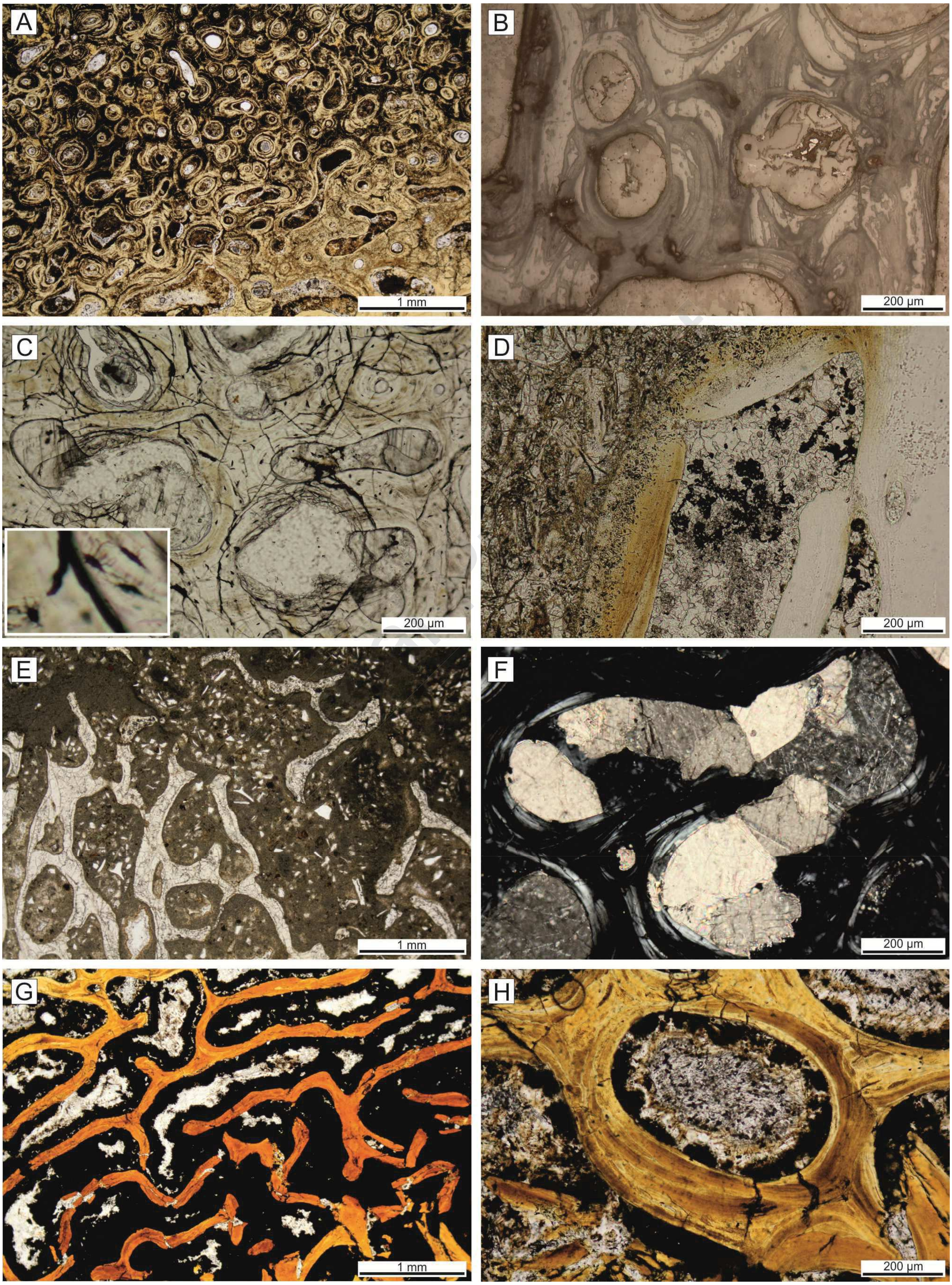

971

972 **Figure 4**

973

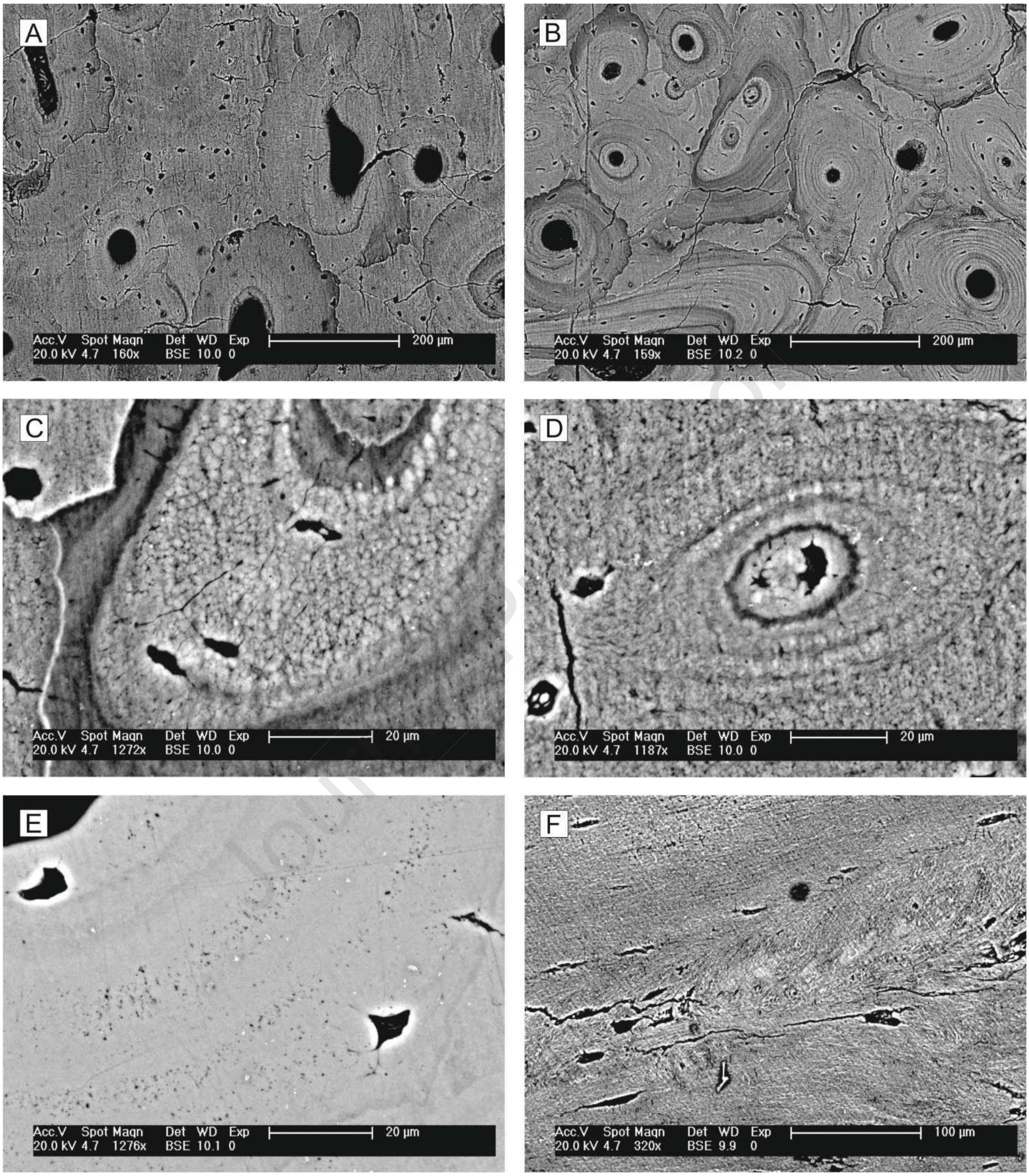

974

975 **Figure 5**

976

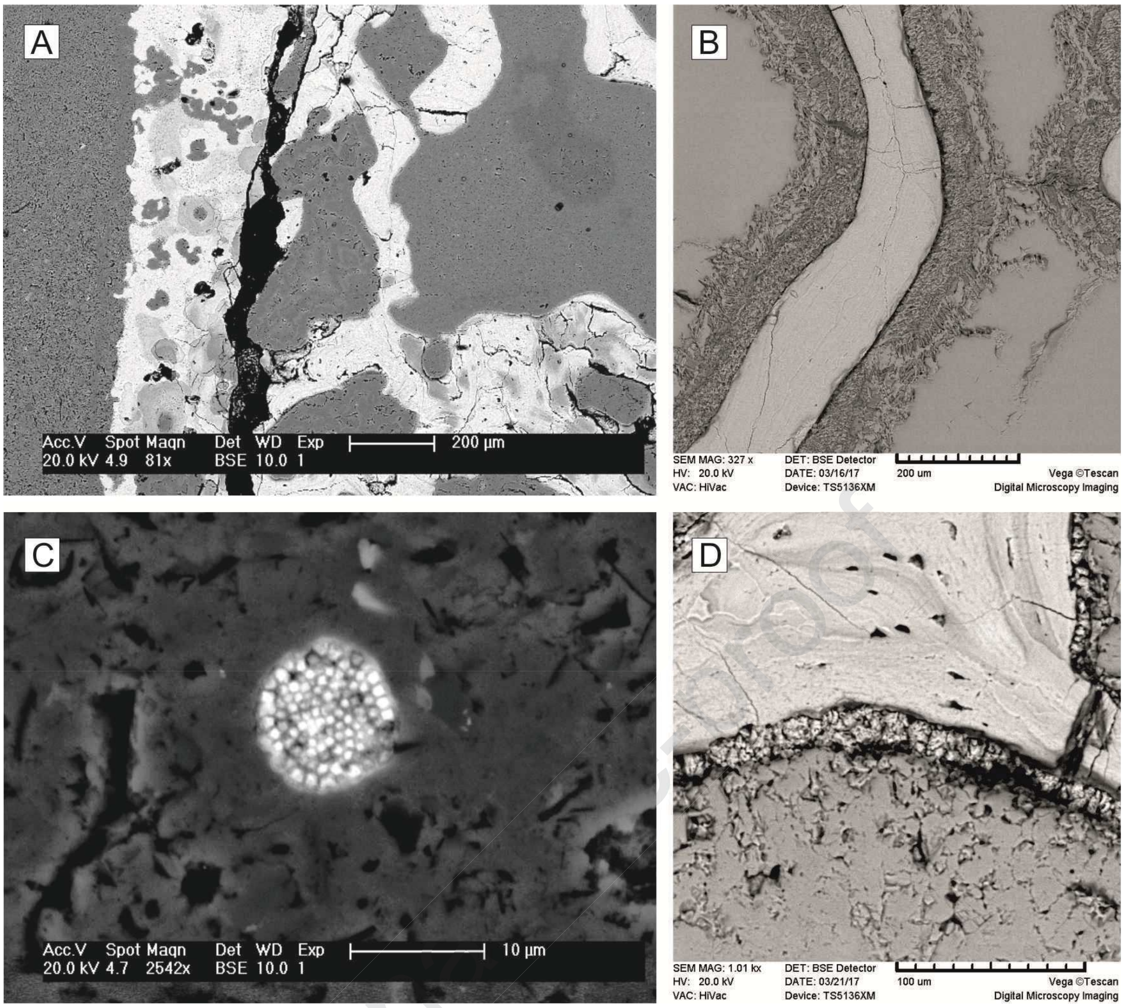
A
Acc.V Spot Magn Det WD Exp 200 µm
20.0 kV 4.9 81x BSE 10.0 1
B
SEM MAG: 327 x DET: BSE Detector
HV: 20.0 kV DATE: 03/16/17 200 um Vega ©Tescan
VAC: HiVac Device: TS5136XM Digital Microscopy Imaging
C
Acc.V Spot Magn Det WD Exp 10 µm
20.0 kV 4.7 2542x BSE 10.0 1
D
SEM MAG: 1.01 kx DET: BSE Detector
HV: 20.0 kV DATE: 03/21/17 100 um Vega ©Tescan
VAC: HiVac Device: TS5136XM Digital Microscopy Imaging

Figure 6

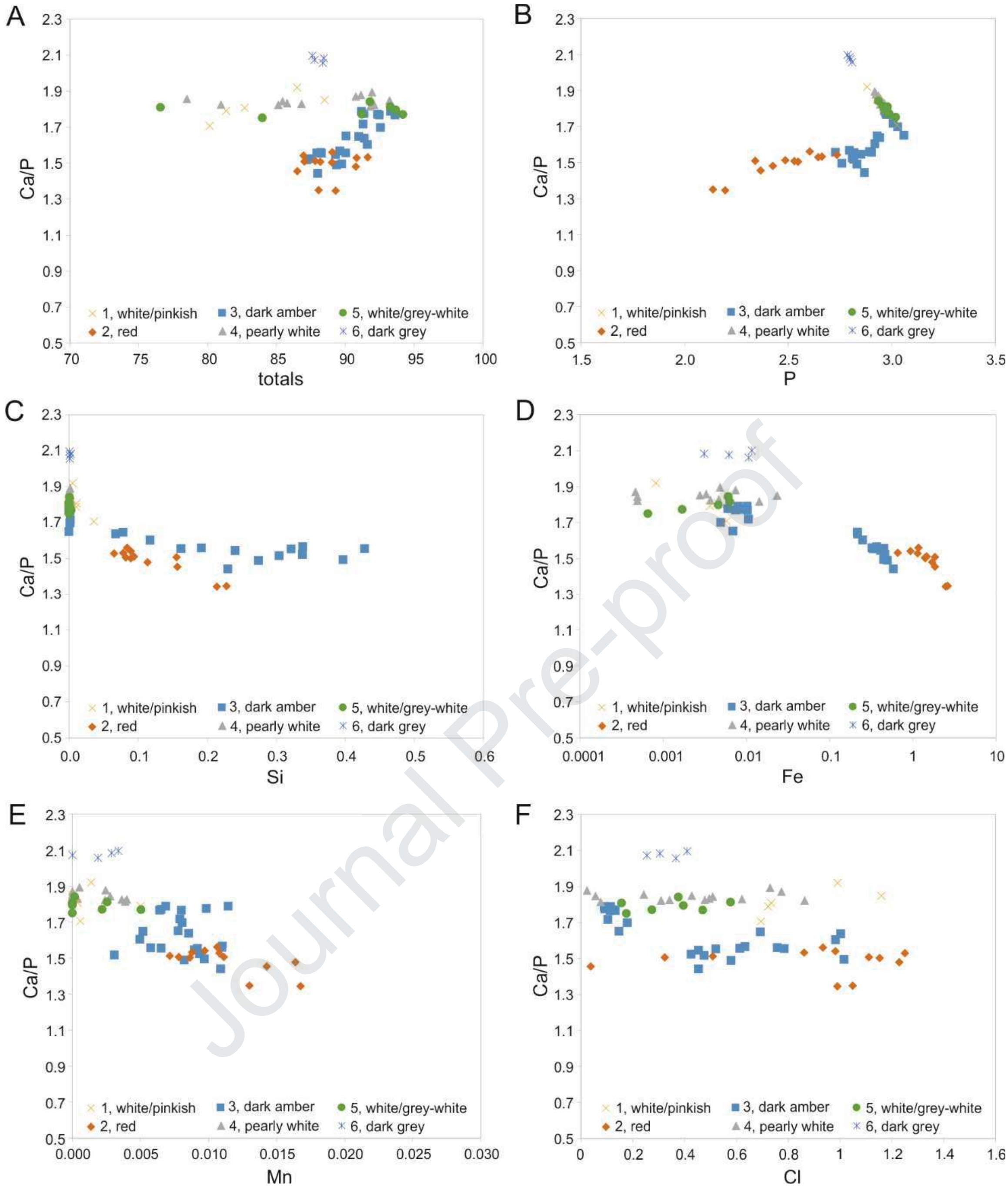
A
B
C
D
E
F
Ca/P
totals
P
Si
Fe
Mn
Cl
1, white/pinkish
2, red
3, dark amber
4, pearly white
5, white/grey-white
6, dark grey

Figure 7

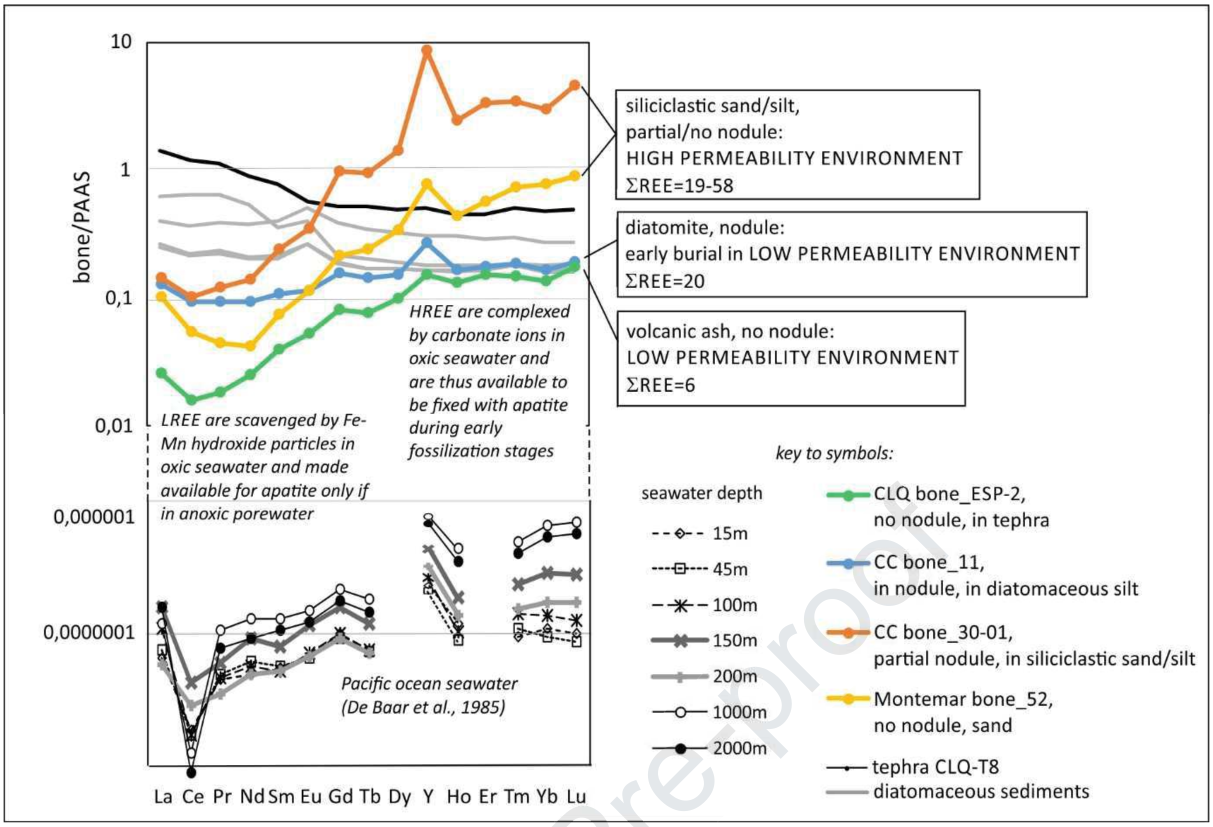

Figure 8

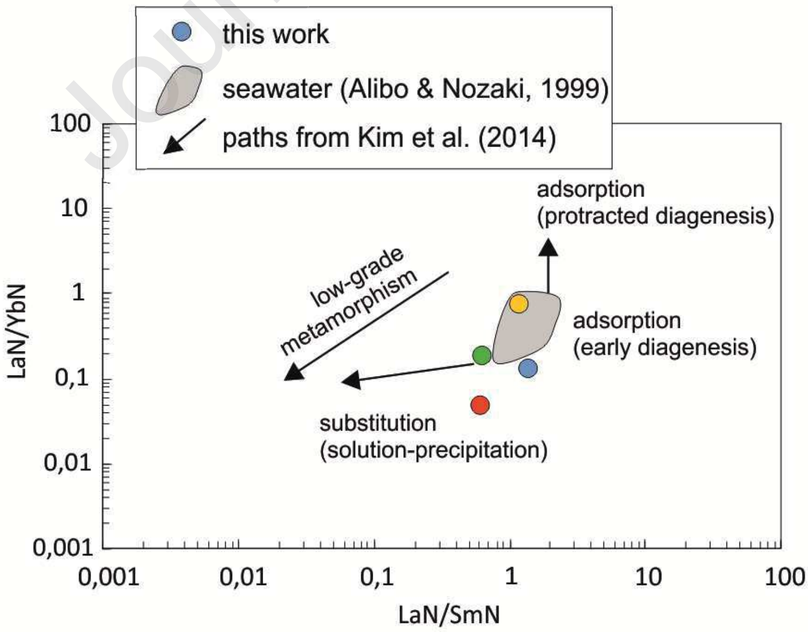

Figure 9

989

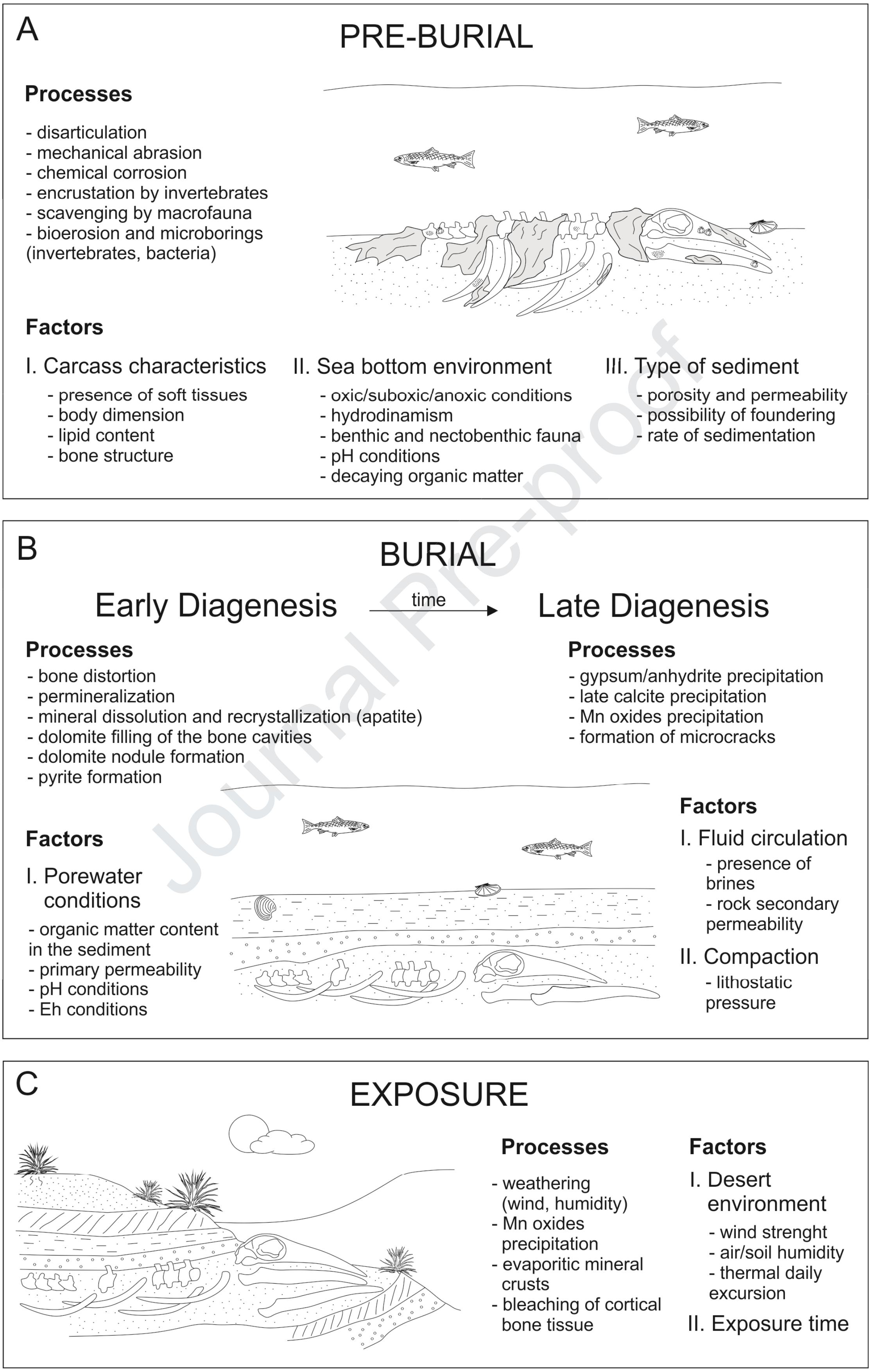

990

991 **Figure 10**

992

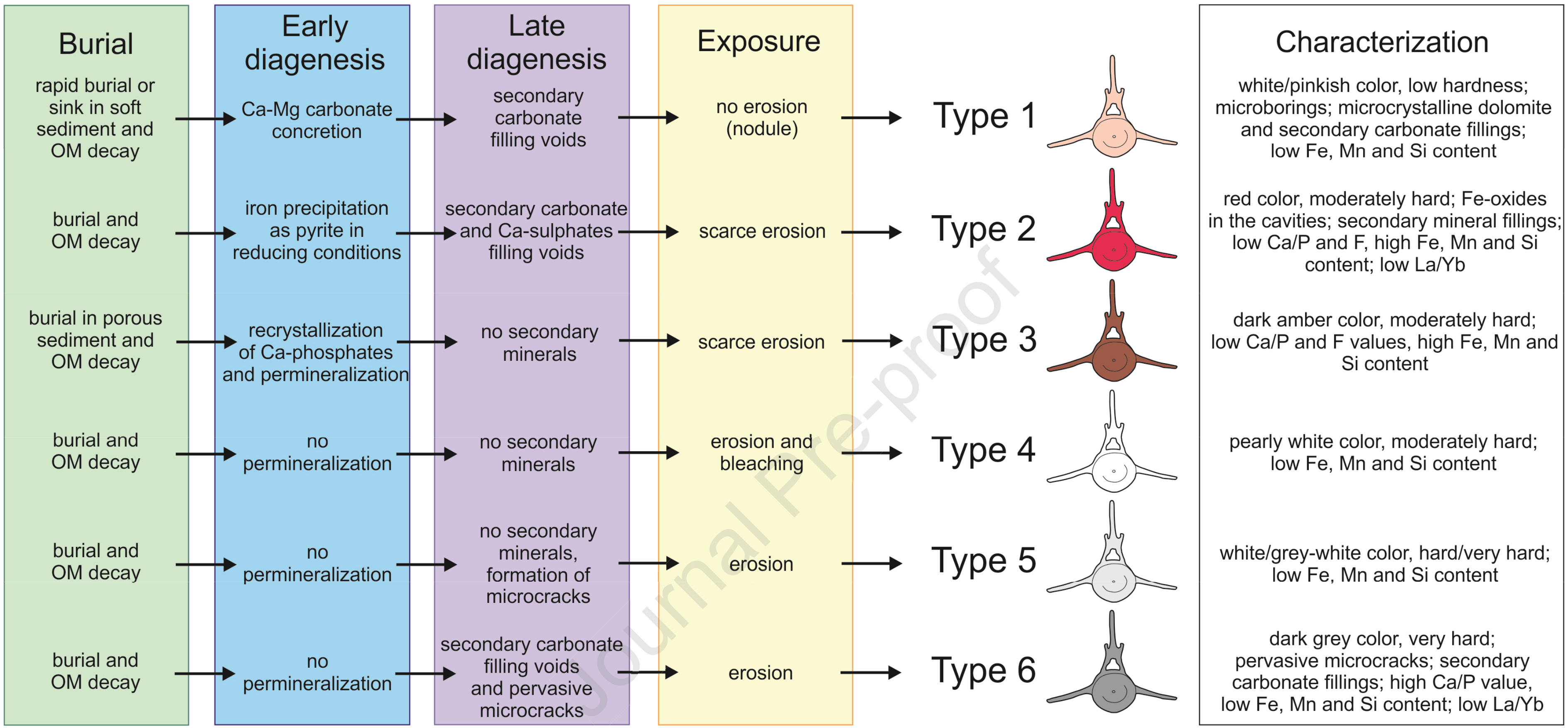

993

Figure 11

Declaration of interests

The authors declare that they have no known competing financial interests or personal relationships that could have appeared to influence the work reported in this paper.